



Modeling of high-speed, methane–air, turbulent combustion, Part I: One-dimensional turbulence modeling with comparison to DNS

Zoltan Jozefik^a, Matthew E. Harvazinski^{b,*}, Venkateswaran Sankaran^c, Sai Sandeep Dammati^d, Alexei Y. Poludnenko^{d,e}, Tianfeng Lu^d, Alan R. Kerstein^f, Rui Xu^{g,1}, Hai Wang^g

^a Jacobs Engineering, Edwards AFB, CA 93524, USA

^b Air Force Research Laboratory, Edwards AFB, CA 93524, USA

^c Air Force Research Laboratory, Wright Patterson AFB, OH 45433, USA

^d School of Mechanical, Aerospace, and Manufacturing Engineering, University of Connecticut, Storrs, CT 06269, USA

^e Department of Aerospace Engineering, Texas A&M University, College Station, TX 77843, USA

^f Consultant, Danville, CA 94526, USA

^g Department of Mechanical Engineering, Stanford University, Stanford, CA 94305, USA



ARTICLE INFO

Keywords:

Turbulent flame

High-speed combustion

One-dimensional turbulence model

Numerical simulations

ABSTRACT

The ability of the one-dimensional turbulence (ODT) model to serve as a surrogate direct numerical simulation (DNS) is assessed for highly turbulent flames. The ODT model is applied to freely propagating premixed methane–air flames at Karlovitz numbers $10, 10^2, 10^3$, and 10^4 , and results are compared with DNS. The ODT model solves the conservation equations for momentum, energy, and species on a one-dimensional domain, which corresponds to a streamwise line of sight spanning the DNS domain. The effects of turbulent advection are modeled via a stochastic process, in which the Kolmogorov and reactive length and time scales are explicitly resolved. Molecular transport and chemical kinetics are concurrently advanced in time. Both the ODT and DNS simulations use a 21-species skeletal chemical model for methane combustion. The accuracy of the ODT model is assessed by comparing its predictions of several key characteristics of the flames for each Karlovitz number tested, including the turbulent flame speed and width and the joint probability density functions (jPDFs) of major and selected minor species as well as the heat release rate conditioned on temperature with the results of DNS under comparable conditions. The ODT model is shown to yield qualitative and quantitative agreement with the DNS data for most of the above flame characteristics. Discrepancies are observed primarily for the jPDFs of several minor species examined. Overall, the ODT approach is shown to be an effective surrogate of DNS, potentially useful for guiding chemical reaction model reduction and for assessing the sensitivities of the flame structure and the burning rate to chemistry under highly turbulent conditions.

Novelty and Significance:

The direct numerical simulations (DNS) of premixed turbulent methane–air flames presented in this work span a uniquely wide range of turbulent intensities, from relatively modest corresponding to Karlovitz number $Ka = 10$ to ultra-high intensities at $Ka = 10^4$. This represents virtually the entire range of turbulent intensities that could be encountered in any realistic situation. This is also the first time that such a wide range of conditions is probed for methane in high-fidelity, fully resolved simulations, which use a fully compressible set of flow equations. The one-dimensional turbulence (ODT) model utilizes the same forcing that is present in the DNS enabling a direct comparison between the ODT and DNS. The results show that ODT captures the key features of the DNS results. ODT is shown to be an effective surrogate for DNS and may be useful in guiding chemical reaction model reduction, where many simulations are required.

* Corresponding author.

E-mail address: matthew.harvazinski.1@us.af.mil (M.E. Harvazinski).

¹ Current address: Department of Chemistry, Stanford University, Stanford, CA 94305, USA; SLAC National Accelerator Laboratory, Menlo Park, CA 94025, USA.

Nomenclature	
Acronyms	
HRR	Heat release rate
Ka	Karlovitz number
Re	Reynolds number
Greek Symbols	
δ_{ij}	Kronecker delta
$\dot{\omega}$	Species mass production rate
η	Kolmogorov length scale
λ	Mixture thermal conductivity
λ_e	Eddy rate
λ_{ke}	Mean occurrence rate of the turbulent kinetic energy injection
μ	Dynamic viscosity
μ_B	Bulk viscosity
ϕ	Equivalence ratio
ρ	Density
σ_{ij}	Deviatoric stress tensor
τ	ODT time scale
τ_{DL}	ODT Darrieus-Landau instability model delay factor
Roman Symbols	
Δh_f	Enthalpy of formation
ΔTKE	Incremental turbulent kinetic energy
Δx	Grid resolution
\bar{M}	Mean molecular weight
\tilde{Y}	Normalized mass fraction
A_c	Nominal cross-sectional area of the ODT domain
C	ODT turbulence intensity
D	Mass diffusivity or diffusion coefficient
E	Total energy
EE	Eddy event
$f(x)$	Triplet map
f_{inj}	ODT eddy injection frequency
h	Sensible enthalpy
h_T	Total enthalpy
j	Species diffusion flux
$K(x)$	Kernel function, $K(s) = x - f(x)$
L	Domain length
l_e	Eddy length
L_{11}	Integral length scale
L_{inj}	ODT eddy injection length scale
l_{\max}	ODT maximum eddy length
N	Number of ODT samples
n	Number of chemical species
P	ODT energy injection rate
p	Pressure
q	Heat flux
S_L	Laminar flame speed
S_T	Turbulent flame speed
S_{ij}	Strain rate tensor, $S_{ij} = \frac{1}{2} \left(\frac{\partial u_i}{\partial x_j} + \frac{\partial u_j}{\partial x_i} \right)$
T	Temperature
t	Time
T_{inj}	Injection eddy turnover time
u	Velocity

U_l	Average turbulent integral velocity, $U_l = U_{rms}/\sqrt{3}$
U_{rms}	Root mean square of turbulence velocity fluctuations
X	Mole fraction
x	Cartesian coordinate
Y	Mass fraction
Z	ODT viscous penalty factor
Superscripts/subscripts	
α	Species number
b	Burned state conditions
u	Unburned state conditions
kin	Kinetic energy
pe	Potential energy
vp	Viscous penalty

1. Introduction

Highly turbulent reacting flows, characterized primarily by high Reynolds numbers, involve a broad range of length and time scales [1]. Together with the large number of chemical species that need to be considered in combustion of hydrocarbon fuels, direct numerical simulations (DNS) of turbulent reacting flows in practical combustors will remain computationally intractable in the foreseeable future [2]. To achieve a feasible computational cost, two primary computational strategies are employed, namely: (1) reduced-order turbulence and combustion models, intended to capture the complex turbulent reacting flow dynamics on smaller sub-filter unresolved scales, and (2) reduced chemical reaction models, which represent complex chemical reaction pathways with a substantially smaller number of species and reactions (e.g., see [3–6]).

The reduction of reaction models is typically carried out using legacy combustion properties as the targets. In particular, laminar flame speed, ignition delay time, and extinction and ignition times in perfectly stirred reactors are some of the widely used properties for sampling possible thermochemical state spaces, and for generating and testing reduced models [6–9]. Yet, as high-intensity turbulence can significantly amplify turbulence-chemistry interactions [1,10] and broaden the thermochemical state structure for a specific mixture composition and temperature [1,11], the thermochemical spaces commonly sampled in reaction model reduction are expected to be notably narrower than those found in highly-turbulent flames. Currently, there has been little to no effort made to bridge the gap between these two thermochemical state spaces. In other areas, efforts have been made to quantify the sensitivity of the turbulent flame response to reaction kinetics using DNS (e.g., see [12]). Yet, because of the associated computational demand, comprehensive sensitivity analysis remains difficult at the DNS level. Therefore, to enable the reaction model reduction and potentially reaction sensitivity screening under highly turbulent conditions, simplified representations of the advective, diffusive, and reactive processes are needed for computational affordability. This is the focus of the current work and of the companion (Part II) article [13].

A variety of approaches for a simplified description of turbulent combustion have been proposed in the literature, but most of them fall short of capturing the full complexity of turbulent combustion. In choosing an appropriate modeling framework, a key requirement for robust turbulent combustion modeling is that the model must be able to access a sufficient portion of the chemical state space [4]. Probability Density Function (PDF) models are advantageous in this regard, but are subject to significant limitations because they do not resolve the flame structure [14]. Flamelet models provide such resolution, but they

rely on low-dimensional manifolds [15]. Thus, neither of these leading approaches is fully satisfactory. Similar considerations apply to other commonly used strategies for turbulent combustion modeling [4,16, 17].

A modeling approach that we find to be well suited to address these challenges is One-Dimensional Turbulence (ODT). ODT resolves the flame structure on a one-dimensional (1D) domain without compromising chemical-state accessibility, and it achieves major cost reduction relative to DNS through the reduced spatial dimensionality [18]. ODT is a fully resolved, unsteady, stochastic model that emulates the Navier-Stokes turbulence. ODT has two key features. First, the properties of the flow reside in a 1D domain. This formulation allows for complete resolution of the interaction between large scales and the molecular transport scales while maintaining computational efficiency. Second, because vortical overturns cannot occur on a 1D domain, turbulent advection is represented using instantaneous mapping events. Unlike Reynolds-averaged Navier-Stokes (RANS) and large-eddy simulation (LES), which model small-scale phenomena while retaining the three-dimensional (3D) representation of the flow, ODT resolves all scales of motion and models the 3D turbulence. A limitation of ODT is that it cannot capture geometric effects and coherent flow structures beyond the so-called eddy events. Yet, as a stand-alone model, ODT has been used to simulate homogeneous turbulent non-reacting [18–23] and reacting flows [24–30]. Notably, for non-premixed [26] and premixed [28] combustion, ODT has provided fundamental insights into the spatio-temporal features of extinction/reignition.

In this paper, we present a systematic ODT modeling study of the premixed methane-air combustion over a wide range of turbulent combustion regimes from the wrinkled flames to broken reaction zones. The benchmark tests use DNS results of the freely propagating premixed methane-air flames at Karlovitz (Ka) numbers of 10, 10², 10³, and 10⁴. As such, this study pursues three goals: (1) Present a detailed description of the globally unstrained, turbulent, methane-air flames over all highly turbulent regimes of practical relevance. This would also allow comparison of the high-Ka methane-air combustion with the combustion of heavy hydrocarbons, in particular, *n*-dodecane, in a similar configuration at Ka = 10², 10³, and 10⁴ presented in an earlier paper [31]. (2) Systematically compare the ODT results to the reference DNS at each of these Ka numbers in order to assess the ODT performance over such an extremely wide range of flow regimes. (3) Finally, our broader goal is to establish ODT as a suitable tool to aid in the reaction model reduction and reaction sensitivity analysis. While the DNS and ODT simulations in the current paper use a 21-species skeletal reaction model of methane combustion, the companion paper [13] demonstrates how the ODT tool facilitates the evaluation of a 12-species reduced methane combustion model for the same reacting flow conditions studied in the current work.

This paper is organized as follows. Section 2 summarizes the mathematical formulations of the ODT method. The chemical kinetic model is presented in Section 3. Section 4 summarizes the physical model, numerical methods, and the computational setup of the DNS. Section 5 describes the configuration and boundary conditions of the ODT calculations. In the results Section 6, we compare ODT model predictions to the DNS data at various Ka numbers. Finally, in Section 7, concluding remarks are provided.

2. ODT modeling approach

A brief overview of the ODT model is given here. Further details can be found in the Appendices, as well as in Refs. [18,29,30,32,33]. The ODT model is derived from the full 3D reacting Navier-Stokes equations. To reduce the cost, the model assumes that variations in all flow quantities occur only in one spatial dimension, *x*, and therefore $\partial \mathbf{Q} / \partial y = \partial \mathbf{Q} / \partial z = 0$, where $\mathbf{Q} = (\rho \ u \ v \ w \ Y_\alpha \ h_T)$. The ODT

model equations for mass continuity, momentum, species, and enthalpy are:

$$\frac{\partial \rho}{\partial t} + \frac{\partial(\rho u)}{\partial x} + EE(\rho) = 0, \quad (1)$$

$$\frac{\partial u_i}{\partial t} + u \frac{\partial u_i}{\partial x} + EE(u_i) = \frac{1}{\rho} \left(-\frac{\partial p}{\partial x} \delta_{ix} + \frac{\partial \sigma_{ix}}{\partial x} \right), \quad (2)$$

$$\frac{\partial Y_\alpha}{\partial t} + u \frac{\partial Y_\alpha}{\partial x} + EE(Y_\alpha) = \frac{1}{\rho} \left(-\frac{\partial j_\alpha}{\partial x} + \omega_\alpha \right) \text{ for } \alpha = 1, \dots, n-1, \quad (3)$$

$$\frac{\partial h_T}{\partial t} + u \frac{\partial h_T}{\partial x} + EE(h_T) = \frac{1}{\rho} \left(\frac{\partial p}{\partial t} + u \frac{\partial p}{\partial x} - \frac{\partial q}{\partial x} + \sigma_{ix} \frac{\partial u_i}{\partial x} \right). \quad (4)$$

In Eqs. (1) - (4), the ODT velocity component *u*, which is aligned with the ODT domain, advects fluid along the domain. This treatment of an ODT velocity profile as an advection velocity was introduced in [29] in order to capture compressibility effects. Eq. (1) forces the development of density fluctuations in an initially constant-density fluid when *u* is not spatially uniform. We solve *n* – 1 species equations and the *n*th species mass fraction is computed using $Y_n = 1 - \sum_{\alpha=1}^{n-1} Y_\alpha$. The remaining terms include the species diffusive flux

$$j_\alpha = -\rho D_\alpha \left(\frac{\partial Y_\alpha}{\partial x} + \frac{Y_\alpha}{M} \frac{\partial \bar{M}}{\partial x} \right), \quad (5)$$

where D_α is the mass diffusivity of species α . A correction velocity is used to ensure that the summation in Eq. (5) is zero. The heat flux is

$$q = -\lambda \frac{\partial T}{\partial x} + \sum_{\alpha=1}^n h_\alpha j_\alpha. \quad (6)$$

The elimination of the derivatives in the *y* and *z* direction only allows for variations along the *x* direction to be considered. This results in a truncated deviatoric stress tensor, for which the three non-zero components are,

$$\sigma_{xx} = \frac{4}{3} \mu \frac{\partial u_x}{\partial x}, \quad \sigma_{yx} = \mu \frac{\partial v}{\partial x}, \quad \sigma_{zx} = \mu \frac{\partial w}{\partial x}. \quad (7)$$

To introduce the effects of turbulence, which are lost by the elimination of the variations in the *y* and *z* directions, the conservation Eqs. (1)–(4) are augmented with a stochastic model. The 3D velocity field and scalar fields evolve in time through both the conservation equations, which account for the molecular evolution, and via a series of stochastic processes. In particular, the term *EE* in Eqs. (1)–(4) is the stochastic eddy event contribution. These instantaneous eddy events are used to represent the action of turbulence in the model. Further details of this can be found in Appendix A.

Conservation equations are supplemented with the ideal-gas equation of state. Thermodynamic properties, transport properties, and chemical reaction rates are calculated using the CANTERA software package [34].

Governing equations are numerically advanced in time using a standard first-order finite-difference discretization subject to an acoustic CFL constraint. Spatial discretization is formally first order on a non-uniform grid used in the current study. An adaptive mesh approach is used, such that the merging and splitting of grid cells is performed in a manner that conserves fluxes of the transported quantities, namely mass, momentum, and energy. For the adaptation, a minimum cell size is set, which corresponds to the DNS grid resolution. Refinement is constrained such that a cell is never more than 2.5 times smaller or larger than a neighboring cell. Local adaptation is based on the gradients of velocity and species and is checked at every time step. A complete description of the adaptation procedure is given by Lignell et al. [35]. The integration of the mean chemical source terms (used in the explicit time advancement) is performed with a higher-order implicit method using the CVODE code of the SUNDIALS package [36].

3. Mixture properties and chemistry model

The reactants mixture considered both in the ODT simulations and in the DNS is a premixed CH₄/air at 30 atm, 700 K, and $\phi = 0.7$. Initial mixture composition and the thermodynamic conditions in the unburned gas were chosen based on a joint consideration of their engine relevance, adequate chemistry sensitization, and as importantly, similarity to the prior DNS of turbulent, *n*-dodecane flames under the same conditions [31], as the current simulations also enable us to compare the flame responses of the two fuels with quite different chemical kinetic characteristics.

Simulations use a skeletal version of the Foundational Fuel Chemistry Model version 1.0 (FFCM1) [37,38], namely the FFCM1-21 model. Briefly, FFCM1-21 is a 21-species, 107-reaction skeletal model derived from the full FFCM1 [38] for the CH₄ combustion. The skeletal model was generated by directed relation graph (DRG) [9] and DRG-aided sensitivity analysis (DRGASA) [39] using autoignition, extinction in perfectly stirred reactors, and 1D laminar flame speeds as targets under a wide range of thermodynamic conditions. Details are provided in the Supplementary Materials of the companion paper [13].

4. DNS physical model and simulation setup

In order to perform the DNS, compressible reactive Navier–Stokes equations are solved on a uniform Eulerian grid using the code Athena–RFX [40]:

$$\frac{\partial \rho}{\partial t} = -\frac{\partial}{\partial x_j} (\rho u_j), \quad (8)$$

$$\frac{\partial(\rho u_i)}{\partial t} = -\frac{\partial}{\partial x_j} (\rho u_i u_j + p \delta_{ij} - \sigma_{ij}), \quad (9)$$

$$\frac{\partial(E)}{\partial t} = -\frac{\partial}{\partial x_j} (Eu_j + pu_j - q_j - u_i \sigma_{ij}) + \rho \Delta h_{f,\alpha} \dot{\omega}_\alpha, \quad (10)$$

$$\frac{\partial(\rho Y_\alpha)}{\partial t} = -\frac{\partial}{\partial x_j} (\rho Y_\alpha u_j - D_{aj}) + \rho \dot{\omega}_\alpha, \quad (11)$$

where σ_{ij} , q_j , and D_{aj} are the viscous stress tensor, diffusive heat flux, and diffusive mass flux, respectively, which are given by:

$$\sigma_{ij} = 2\mu(S_{ij} - \frac{1}{3}\theta\delta_{ij}) + \mu_B S_{kk} \delta_{ij}, \quad (12)$$

$$q_j = \lambda \frac{\partial T}{\partial x_j} - \rho \dot{\omega}_\alpha D_{aj}, \quad (13)$$

$$D_{aj} = \rho D_\alpha \frac{Y_\alpha}{X_\alpha} \frac{\partial X_\alpha}{\partial x_j} \quad (\text{no summation over } \alpha). \quad (14)$$

The equation of state is that of an ideal gas.

Athena–RFX has been extensively used to study a wide variety of problems involving reacting turbulence [41–43], turbulent flames [31, 40,44–47], and detonations [48,49]. The numerical flow solver in Athena–RFX [40] employs a directionally unsplit, corner transport upwind (CTU), finite volume scheme with the piecewise parabolic interpolation (PPM) for spatial reconstruction [50]. Fluxes at cell interfaces are evaluated by solving the local Riemann problem using the HLLC Riemann solver.

The chemical reactions and the thermodynamic functions of chemical species are computed using the skeletal FFCM1-21 mechanism and its associated thermochemical database, as described in Section 3. A non-iterative, single-step, semi-implicit ordinary differential equation (ODE) integrator YASS is used to solve the stiff system of equations for chemical kinetics [51]. The chemical source terms are coupled to the flow equations using Strang splitting method [52]. The overall solver is 2nd-order accurate in time and 3rd-order accurate in space. To improve the run-time performance, specialized source code for the chemical reaction terms is automatically generated from the standard CHEMKIN [53] input files in a preprocessing step and subsequently compiled into Athena–RFX. The preprocessor generates code that

Table 1

DNS parameters: Karlovitz number, domain dimensions, as well as grid size and resolution, Δx .

Ka	L_x [mm]	L_y [mm]	L_z [mm]	N_x	N_y	N_z	Δx [μm]
10	0.671	0.671	10.74	256	256	4,096	2.6
10^2	0.671	0.671	10.74	256	256	4,096	2.6
10^3	0.671	0.671	5.37	512	512	4,096	1.3
10^4	0.168	0.168	1.34	512	512	4,096	0.33

evaluates the rates of change of the species mass fractions and temperature due to chemical reactions along with their analytical Jacobian generally following the formulation of Perini et al. [54]. Polynomials for the mass-specific internal energy and constant-volume heat capacity are directly evaluated to solve for temperature given the conservative solution.

Coefficients of the species shear and bulk viscosity as well as binary diffusion are evaluated from the kinetic theory expressions [55]. Thermal conduction coefficients of pure species are evaluated using expressions given by Warnatz [56]. Mixture-averaged conduction and viscosity coefficients are computed using averaging formulas of order 1/4 and order 6, respectively, as recommended by Ern & Giovangigli [57]. Mixture-averaged diffusion coefficients for each species are computed as in the Sandia TRANSPORT library [58].

DNS of the freely propagating flames are carried out in a traditional “flame-in-a-box” configuration [31,40,44,59] in a 3D domain with dimensions $L_x \times L_y \times L_z$. Here, the z -direction is the mean flame propagation (streamwise) direction, while x and y represent the transverse directions. The domain is initially filled with the unburned mixture with properties given in Section 3. All boundary conditions are initially set as periodic. The turbulence in the domain is sustained by adding isotropic, solenoidal (divergence-free), large-scale velocity perturbations to the velocity field using a spectral method [40,44]. The turbulence is then allowed to evolve for two large-scale eddy turnover periods, τ_{ed} , to reach a statistically steady state. Here we define $\tau_{ed} = L/U_L$ as the ratio of the domain width, $L = L_x = L_y$, to the corresponding turbulent velocity at the scale of the domain width, U_L . After that, laminar flame profile corresponding to the fuel-air mixture (obtained using the PREMIX code [60]) is superimposed on the velocity field in the domain, and the flame is allowed to evolve for another large eddy turnover time before statistics are collected for analysis. Once the flame is initialized, the streamwise boundary conditions are changed from periodic to zero-order extrapolation to allow fluid and any pressure waves introduced to exit the domain.

For the cases studied using DNS, Table 1 shows L_x , L_y , and L_z , as well as grid size, N_x , N_y , and N_z , and resolution, Δx , and the resulting Karlovitz numbers, Ka, defined as the ratio of the chemical timescale to the Kolmogorov timescale. The integral-scale Reynolds number, Re, and the Kolmogorov scale, η , in the unburnt and burnt mixtures, along with the integral length scale, L_{11} , the r.m.s. velocity, U_{rms} , and the associated large-scale eddy turnover time, τ_{ed} , are shown in Table 2. Due to the increased grid resolution requirements for $Ka = 10^4$, the integral length is decreased from 0.158 mm to 0.04 mm in this case to make DNS computationally affordable. We also modeled the $Ka = 10^4$ case for the same integral scale L_{11} as in $Ka = 10$, 10^2 , and 10^3 cases using only ODT due to the high computational cost of the DNS in a domain of this size. Parameters for this ODT calculation are given on the last line of Table 2.

5. ODT setup

The ODT domain is a line-of-sight through the 3D DNS domain, aligned with the mean direction of flame propagation in the DNS (denoted as the z -direction in DNS and the x -direction in ODT). In the direction of propagation, both the DNS and ODT have inflow/outflow boundary conditions. In the absence of the viscous penalty parameter,

Table 2
Relevant characteristic turbulent scales in simulations for different Ka .

Ka	Re_u	Re_b	η_a [μm]	η_b [μm]	$\eta_a/\Delta x$	$\eta_b/\Delta x$	L_{11} [mm]	U_{rms} [m/s]	τ_{ed} [μs]
10	110	17	6.5	25.8	2.5	9.92	0.158	2.46	310.66
10^2	512	81	2.0	8.2	0.77	3.15	0.158	11.41	67.401
10^3	2,545	401	0.6	2.6	0.5	2.0	0.158	53.21	14.527
10^4	1,779	280	0.2	0.8	0.6	2.42	0.040	155.57	1.245
10^4 -large L_{11}	11,557	1,822	0.2	0.8	—	—	0.158	—	—

Table 3
ODT turbulence forcing parameters.

Ka	P [kJ/m ³ s]	L_{inj} [mm]	f_{inj} [1/ms]	l_{max} [mm]
10	2.8	0.4	200	0.671
10^2	75	0.3	2,800	0.671
10^3	2,800	0.3	3,000	0.671
10^4	100,000	0.06	90,000	0.168
10^4 -large L_{11}	120,000	0.3	13,000	0.671

the eddy selection process can generate arbitrarily small eddies due to the mesh adaptation. To prevent this from occurring, the viscous penalty can be set to a small positive number, or alternatively, the mesh adaption can be constrained with a minimum cell size, below which further adaptation is not allowed. This minimum cell size will then enforce a lower bound for the eddy size. The use of the viscous penalty is advantageous for predictive parameter studies because the viscous-penalty term is a physics-based non-dimensional group, which encapsulates the parameter dependencies of the viscous cutoff. This however requires tuning of the value of the viscous penalty factor. Since the focus of this study is comparison between the ODT and DNS, we adopt the DNS value of the minimum cell size in ODT and thus avoid the need to tune the penalty factor. The advantage of using a minimum cell size, which is the same in the ODT and DNS, is that it ensures a degree of numerical consistency between ODT and DNS for comparison purposes. This is analogous to setting the maximum eddy size, l_{max} , equal to the DNS domain width.

Stationary, forced, homogeneous, isotropic turbulence is generated in the ODT domain with the goal of keeping the turbulent kinetic energy constant in the system. The ODT implementation was developed by Fistler et al. [61]. Details of the current implementation can be found in Appendix B. Table 3 summarizes the forcing parameters used in the simulation for each of the Ka values considered. The parameters are the energy injection rate, P , scale, L_{11} , and frequency, f_{inj} , as well as the maximum eddy size, l_{max} . The parameters are set independently for each Ka to ensure that the total kinetic energy and integral length scale of a given ODT simulation match the corresponding DNS simulation. Other traditional ODT parameters remain fixed for each simulation. Specifically, the turbulence intensity parameter is set to 50, the Darrieus-Landau instability model delay factor is set to 0.1, and the viscous penalty is set to zero.

Each ODT calculation is based on an ensemble size of 80. The size of the ensemble was determined by examining ensembles with 20, 40, and 80 realizations and verifying that the computed metrics and statistics showed no appreciable difference between 40 and 80 realizations.

6. Results and discussion

6.1. Structure of fast CH₄ /air turbulent flames

We first describe the properties of the 3D freely propagating turbulent flames studied in the DNS. Fig. 1 illustrates the flame structures computed at the four Ka values. These calculations span four orders of magnitude in turbulent intensity corresponding to effectively all combustion regimes of practical relevance: from relatively low-speed conditions, $Ka = 10$, which are typically associated with the corrugated flamelet regime of combustion, to ultra-high intensities, $Ka = 10^4$, well into the broken, or distributed, reaction zone regime. Fig. 2 shows the

temperature, normalized heat release rate (HRR) per unit volume, and normalized mass fractions of CH₂O, \tilde{Y}_{CH_2O} , and CO, \tilde{Y}_{CO} , for each of the Ka values. Each panel is a 2D cut through the center plane of the respective DNS domain. The temperature fields (Fig. 2a) characterize the overall flame structures. The fields of normalized HRR and \tilde{Y}_{CH_2O} and \tilde{Y}_{CO} illustrate the structure of the reaction zone. In particular, CH₂O can be associated with the earlier stages of fuel oxidation, while the CO distributions are related to the rate-controlling CO to CO₂ conversion. Pronounced changes can be seen in the flame structure as the turbulence intensity increases, as will be discussed in details below. Such changes are reflective of the turbulence-combustion coupling, and they determine the corresponding changes in the global flame properties, in particular, its burning speed, and the propensity to local or global extinction. Such a broad range of turbulent conditions is subsequently used to assess the accuracy of the ODT model.

At the lowest intensity studied, $Ka = 10$, the flame brush consists almost exclusively of highly corrugated flamelets with pockets of unburned reactants. Under the conditions shown, the laminar flame width is only ~ 6 times the Kolmogorov scale in the unburned gas, and ~ 1.6 times larger in products because of an increased viscosity and anisotropic fluid expansion across the flame [41]. As a result, the ability of the smallest eddies of size η to enter the flame and disrupt it is limited, and the local flame structure remains close to that of a laminar flame. Fig. 2b shows that heat release is confined to thin filaments associated with laminar flamelets, and it is relatively uniform along the flame front. HRR values are close to those in the laminar flame with the exception of regions with high curvature. The thin filamentary structure of the reaction zone, and its overall uniformity, can also be seen in \tilde{Y}_{CH_2O} and \tilde{Y}_{CO} (Figs. 2c and 2d at $Ka = 10$).

At $Ka = 10^2$, the flame becomes disrupted by turbulence with the preheat zone broadened (Fig. 2a) and the heat release zone (Fig. 2b) less well defined than at $Ka = 10$. A relatively narrow region of heat release though can still be identified. Distributions of mass fractions of CH₂O and CO appear only locally broadened (Fig. 2c and 2d). Hence, in contrast to the nominal view that flames at $Ka = 10^2$ should approach the broken reaction zone regime, the current simulation suggests that even such fast turbulence is still unable to fully disrupt the reaction zone. This result is supported by observations made earlier for the single-step chemistry flames [40,41] and in more realistic and complex mixtures, such as H₂/air and CH₄/air [59], as well as *n*-dodecane/air [31] under similar turbulent conditions.

Further increase in turbulent intensity to $Ka = 10^3$ results in a disruption of the reaction zone in addition to the preheat zone. The overall flame structure is now representative of the broken flame regime. Here, the Kolmogorov scale in the unburned gas is only 1/64 of the thermal flame width. As a result, the thin filamentary structure of the HRR is replaced with a collection of disjoint patches and islands of exothermicity (Fig. 2c at $Ka = 10^3$), with a similar structure also seen in \tilde{Y}_{CH_2O} and \tilde{Y}_{CO} . The magnitude of the heat release is quite non-uniform with regions of both low and high heat release being present.

Ultra-high intensity regimes exemplified by $Ka = 10^4$ have been observed recently in flames of hydrogen [59], methane [59], and *n*-dodecane [31]. This extreme condition represents a poorly explored area of premixed reacting flows. At these turbulent intensities, the Kolmogorov scale in cold reactants is 256 times smaller than the laminar flame width resulting in rapid turbulent mixing. The temperature field shows further spreading of the overall turbulent flame relative to the

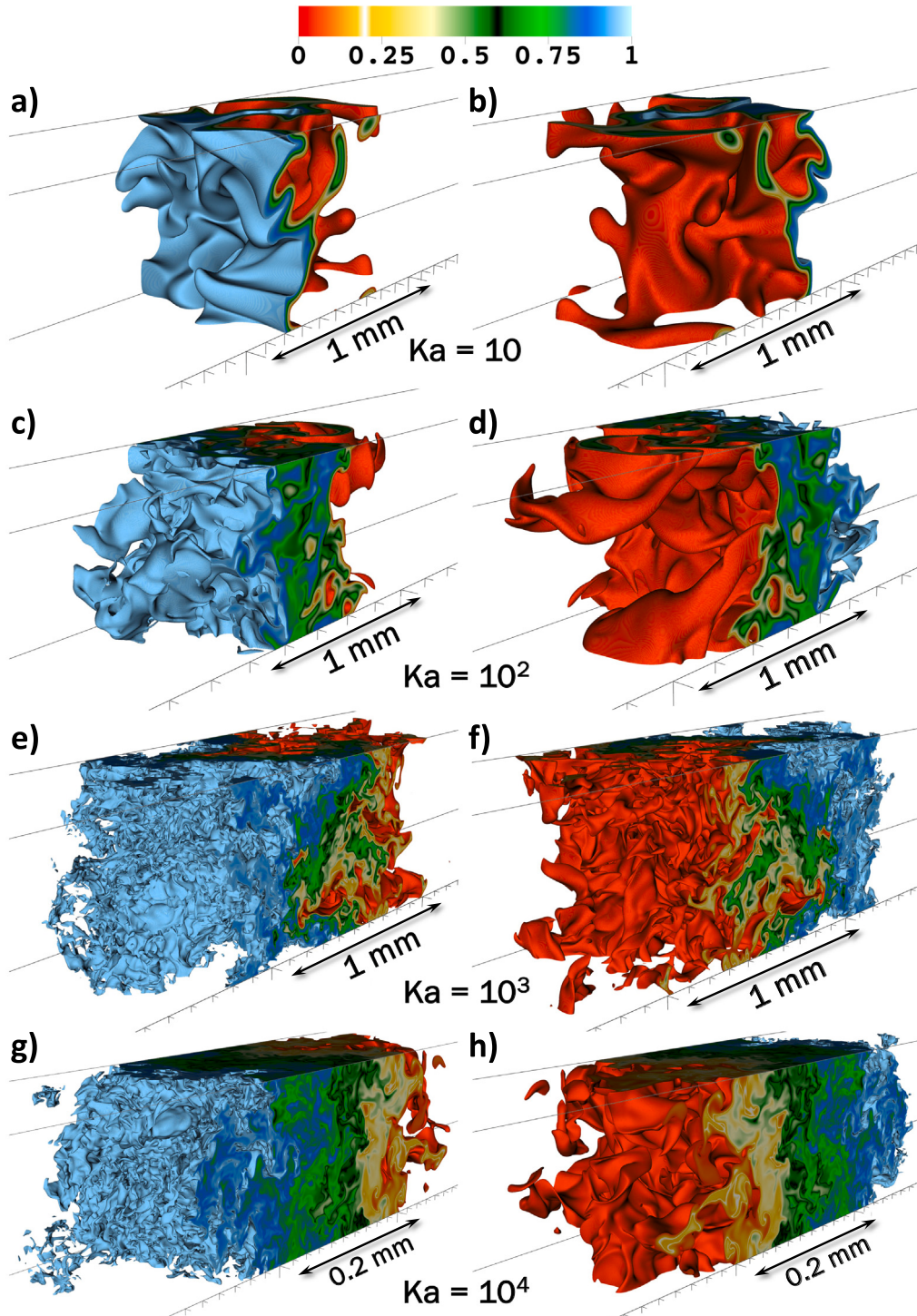


Fig. 1. Structure of the 3D freely propagating turbulent CH_4/air flames in a canonical “flame-in-a-box” DNS at different Ka . Shown are the isovolumes of the fuel mass fraction normalized by its maximum value in the laminar flame, $\bar{Y} = 0.05\text{--}0.95$. Panels (a), (c), and (g) show the view of the turbulent flame from the fuel side, while panels (b), (d), and (h) show the view of the turbulent flame from the product side.

$\text{Ka} = 10^3$ case (Fig. 2a at $\text{Ka} = 10^4$). Some of this observation is due to the amplified spatial scale. The two most notable differences are in the HRR and CH_2O and CO mass fractions. The overall distribution of HRR is smoother and the islands of localized heat release seen at $\text{Ka} = 10^3$ are no longer visible at $\text{Ka} = 10^4$. The local HRR values are substantially lower. Similar changes can be seen in the distributions of species mass fractions. Both $\bar{Y}_{\text{CH}_2\text{O}}$ and \bar{Y}_{CO} show lower local values at $\text{Ka} = 10^4$ than at $\text{Ka} = 10^3$. This clearly indicates the pronounced changes in the local thermochemical state within the turbulent flame as it moves away from

that of a locally discernible flamelet to one that is more characteristic of a well-stirred reactor.

Flame response to the high turbulence intensity at $\text{Ka} = 10^4$ is quite different between methane and *n*-dodecane flames at comparable conditions. For example, the reduction of the local HRR seen in the CH_4/air flame is not observed in a comparable *n*-dodecane-air flame. Instead, the turbulent *n*-dodecane-air flame shows a much higher exothermicity than its laminar counterpart (cf. Fig. 7 of [31]). Furthermore, distributions of the HRR and CH_2O mass fraction in the *n*-dodecane/air flame

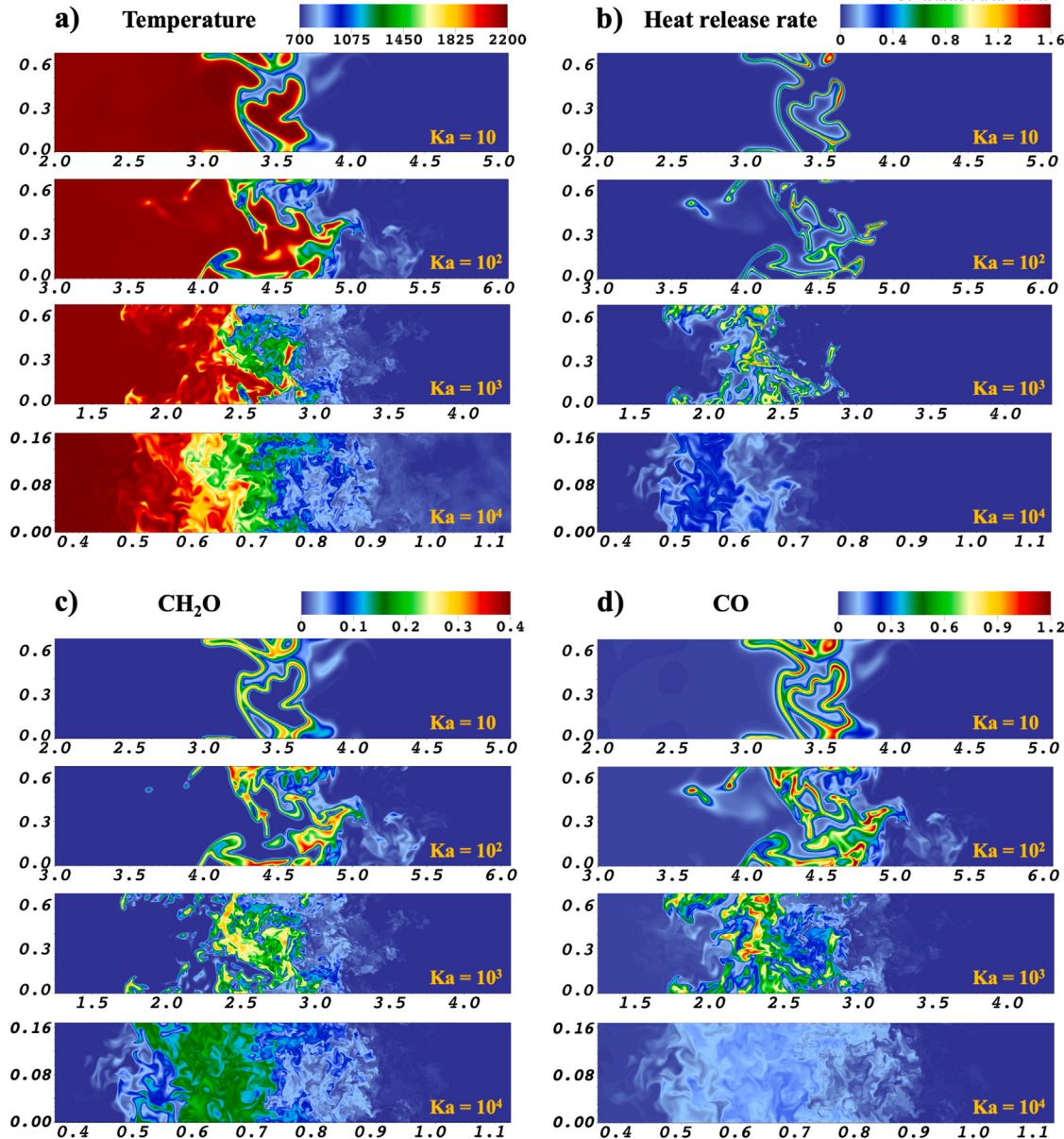


Fig. 2. Temperature (a), heat release rate (b), $\tilde{Y}_{\text{CH}_2\text{O}}$ mass fraction, \tilde{Y}_{CO} (c), and CO mass fraction, \tilde{Y}_{CO} (d) in DNS of CH_4 /air flames at 30 atm, 700 K, and $\phi = 0.7$ at different Ka . Quantities in panels (b), (c), and (d) are normalized by the corresponding peak values in the laminar flame profile calculated for the instantaneous upstream flow pressure and temperature, namely the normalization constants are (b) $8.7 \times 10^{14} \text{ erg/g s}$ ($\text{Ka} = 10$), $8.8 \times 10^{14} \text{ erg/g s}$ ($\text{Ka} = 10^2$), $8.9 \times 10^{14} \text{ erg/g s}$ ($\text{Ka} = 10^3$), and $9.8 \times 10^{14} \text{ erg/g s}$ ($\text{Ka} = 10^4$), (c) 6.7×10^{-4} , and (d) 1.6×10^{-2} . Shown are the 2D slices through the middle of the computational domain. Note that the domain in the $\text{Ka} = 10^4$ case is four times smaller than at lower Ka .

were significantly less uniform at $\text{Ka} = 10^4$ than in the CH_4 /air flame (cf. Fig. 6 of [31]). While a discussion of the cause of these differences is beyond the scope of the current paper, the differences nevertheless highlight the effect of chemistry on the structure of turbulent flames under the high-pressure, high- Ka conditions tested.

The change in the flame properties with increasing Ka is further illustrated in Fig. 3, which summarizes the time-averaged turbulent flame burning speeds based on the fuel consumption rate, S_T/S_L , [40] for all four Ka values. Here the laminar flame speed S_L is calculated based on the corresponding average instantaneous temperature and pressure of the unburned mixture. Such correction is important to properly account for the flow heating due to the turbulent energy dissipation, which can be quite substantial at high turbulent intensities [31,40]. In the figure, the turbulence intensity is represented by the average turbulent integral velocity in the upstream cold flow normalized by the same laminar flame speed, i.e., U_I/S_L .

Fig. 3 shows that the flame burning velocity exhibits the characteristic “bending phenomenon” previously reported in the literature [62],

[63], which represents a departure from Damköhler scaling with increasing turbulent intensity. In the low-speed regime with $\text{Ka} = 10$, S_T/S_L is predominantly determined by the instantaneous total area of the temperature isosurface corresponding to the peak reaction rate [40]. The impact of thermodiffusive effects is minimal since the Lewis number, Le , for CH_4 /air at $\phi = 0.7$ is close to unity [64]. As U_I increases, the growth of S_T slows down.

Fig. 3 also shows S_T/S_L for four *n*-dodecane/air flames taken from [31]. At $\text{Ka} = 10$, S_T/S_L is lower for the *n*-dodecane flame due to differences in the thermodiffusive properties associated with high $\text{Le} \approx 4$ of lean *n*-dodecane mixtures [64]. *n*-Dodecane flames also exhibit bending phenomena with the S_T/S_L growth slowing at higher Ka , albeit to a significantly lesser extent than for methane. As a result, at $\text{Ka} \gtrsim 65$, burning speed for *n*-dodecane becomes larger than for methane, finally exceeding S_T/S_L for CH_4 by almost a factor of 2.5 at $\text{Ka} = 10^4$.

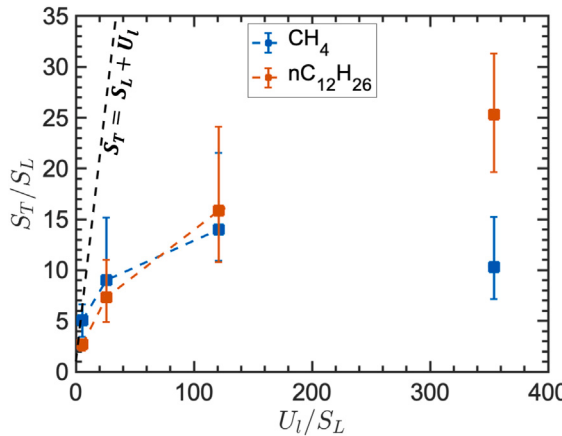


Fig. 3. Normalized turbulent flame speed S_T/S_L as a function of the normalized turbulence intensity U_l/S_L for methane/air flame (this study). Also included in the figure are the turbulent flame speed values of the *n*-dodecane/air flames [31] under comparable conditions of 700 K unburnt gas temperature, 30 atm pressure, and equivalence ratio $\phi = 0.7$. The values of U_l are based on the RMS turbulence velocity fluctuation values, U_{rms} , given in Table 2. Error bars represent one standard deviation of the values of S_T observed in the course of the time-averaging interval and they demonstrate the degree of variability of S_T .

It is important to emphasize that the values of S_T for $Ka = 10^4$ should not be compared directly to those at $Ka = 10^3$. Due to the resolution constraints, the computational domain for this case was one-quarter of the domain size of the other three cases. This limited the flame width, which is typically comparable to the turbulent integral scale [40,65]. This raises the question regarding the values of S_T at $Ka = 10^4$ if the turbulent integral scale were equal to that in the lower-speed cases. In particular, if a four times larger integral scale results in a proportional increase of the flame width and thus flame burning volume, this would result in a similar increase in fuel consumption rate and thus S_T . If that were the case, we expect to see $S_T/S_L \sim 40$ at $U_l/S_L \approx 360$ ($Ka = 10^4$) (above and outside Fig. 3), a dramatic rise of the flame burning speed and a break in the bending trend of S_T , despite the spatially broader, but lower overall local HRR values.

The extremely high computational cost of a DNS calculation at $Ka = 10^4$ in such a large domain precludes us from testing the above projection in DNS, although this projection is supported by a recent study of Aspden et al. [59] (hereafter, ADB19). That work also considered fast turbulent flames in CH_4/air mixtures at comparable Ka from 108 to 8767 using a similar “flame-in-a-box” setup with externally forced turbulence. The flame structure described in that work at $Ka = 8767$, however, is different from the one discussed above. In particular, ADB19 do not find HRR suppression at high Ka , and instead they see a slight increase of the HRR (cf. Fig. 6c in ADB19). Furthermore, the distribution of the HRR is much more filamentary and less uniform than that shown in Fig. 2b even though the field of $Y_{\text{CH}_2\text{O}}$ is qualitatively similar to the one shown in Fig. 2c.

In presenting this comparison, two important differences must be emphasized between the simulations described here and those in the work of ADB19. First, ADB19 considered atmospheric conditions in contrast to the high pressure, high temperature condition considered here. Second, the numerical solver used by ADB19 is a low-Mach-number formulation [66] in contrast to a fully compressible solver in Athena-RFX. Such difference in the formulation of the flow equations becomes important at high Ka , where compressibility effects are significant due to the high turbulent Mach numbers, Ma_t . For instance, in the $Ka = 10^4$ case, $\text{Ma}_t = 0.26$, which places it in a compressible turbulent regime. A low-Mach-number solver also does not allow for dissipative

heating of the flow, which is important in fast turbulence as discussed above.

Despite these differences, ADB19 find that S_T/S_L shows bending between $Ka = 1$ and 10^2 , however it increases rapidly for $Ka \sim 10^3$ and 10^4 , suggesting that flames in ultra-fast turbulence may indeed experience rapid growth of the burning speed, which would result in a characteristic S-shape of the S_T curve instead of its monotonic bending down. Based on Fig. 3, it can be hypothesized that such growth would be significantly larger for heavy hydrocarbon fuels, such as dodecane, compared to CH_4 . Confirming this prediction is a subject of future work.

Physical mechanisms controlling S_T in ultra-fast turbulence are associated with an intricate interplay between local extinction, radical pool formation, and reignition as was discussed in [31]. Analysis of these processes is beyond the scope of this paper, and it will be presented in a separate study. Here, we simply hypothesize this possibility based on the DNS calculations with a smaller integral scale, and we shall test this projection with an ODT calculation in Section 6.2.6 below.

6.2. ODT turbulent flame properties

Spatial profiles of a laminar freely propagating flame were computed first using the ODT code and compared to results from the PREMIX code [60]. Results, shown in Fig. S1, are in close agreement with each other, thus providing a demonstration of the accuracy of the ODT solver and the implementation of the chemistry model.

6.2.1. Turbulence calibration

We first show in Fig. 4 the integral length scale, L_{11} , and the total r.m.s. velocity, U_{rms} , as a function of time for the four Ka cases. The U_{rms} is calculated from the three velocity components. An ensemble average of 80 ODT realizations is used to compute the integral length scale and U_{rms} . Values reported are an average over the entire spatial domain. Target values are taken from the DNS after the turbulence has become fully developed. They are used to ensure that the total kinetic energy and turbulence scales in ODT are close to those in the corresponding DNS. In the DNS, the integral length is approximately 0.15 mm for $Ka = 10$ to 10^3 . Results in Fig. 4 show that the target integral length values are approximately achieved and maintained for the duration of the ODT simulations using the forcing parameters in Table 3. The percent differences in the mean integral length scale between the DNS and ODT are 6.6%, 2.8%, 5.0% and 24.2% for $Ka = 10, 10^2, 10^3$, and 10^4 respectively. The r.m.s. velocity in DNS is 200, 1000, 4700, and 14,000 cm/s for $Ka = 10, 10^2, 10^3$, and 10^4 , respectively. The r.m.s. velocity in ODT is 200, 850, 4150, 12,650 cm/s for $Ka = 10, 10^2, 10^3$, and 10^4 , respectively. In the ODT model, the forcing of turbulence maintains constant kinetic energy for the duration of the simulation, and together with the integral length scale this ensures that turbulence in ODT is comparable to that in DNS.

6.2.2. Instantaneous spatial profiles

Here, we discuss the instantaneous streamwise profiles of temperature, heat release rate, and major and minor species mass fractions in the ODT simulations. All results correspond to the fully developed turbulent conditions. Strong similarities are observed when comparing the DNS fields of temperature and HRR (Fig. 2) with the profiles from ODT shown in Fig. 5. Quantitative comparisons of the flame width in DNS and ODT are given later. Qualitatively, the flame width values, estimated from the ODT temperature profiles, are comparable to those in DNS for each Ka . Furthermore, HRR in DNS and ODT shows qualitatively similar behavior at each Ka . At $Ka = 10$, ODT shows three burning fronts. At $Ka = 10^2$, the ODT heat release region broadens. At $Ka = 10^3$, broad regions of low heat release rate are observed, indicating rapid mixing of fluid elements. Lastly, at $Ka = 10^4$, we observe reduced HRR.

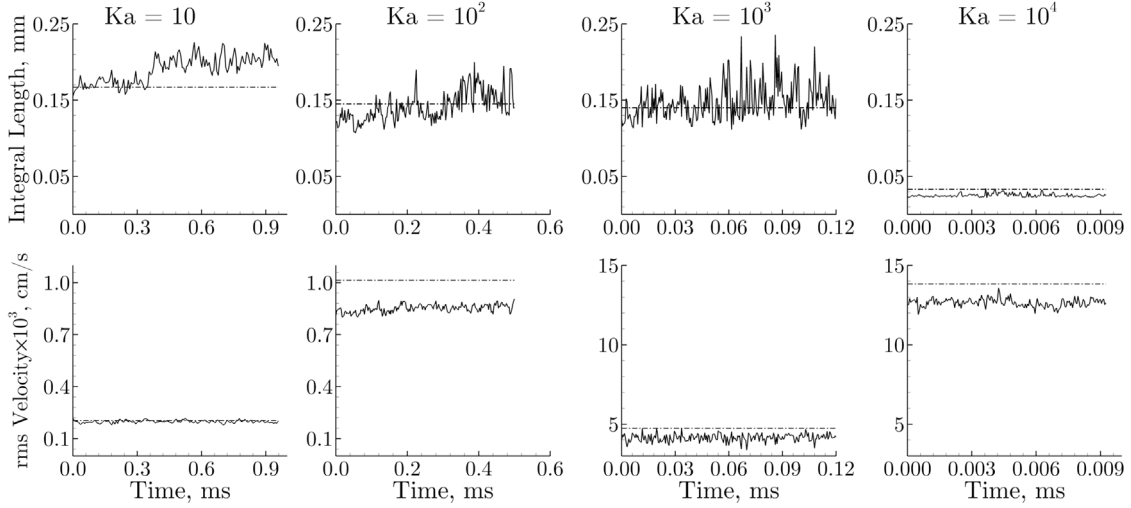


Fig. 4. Integral length scale (top panels) and total r.m.s. velocity (bottom panels) as a function of time. The horizontal dashed lines denote the respective target DNS-based integral length and r.m.s. velocity for a given Ka value.

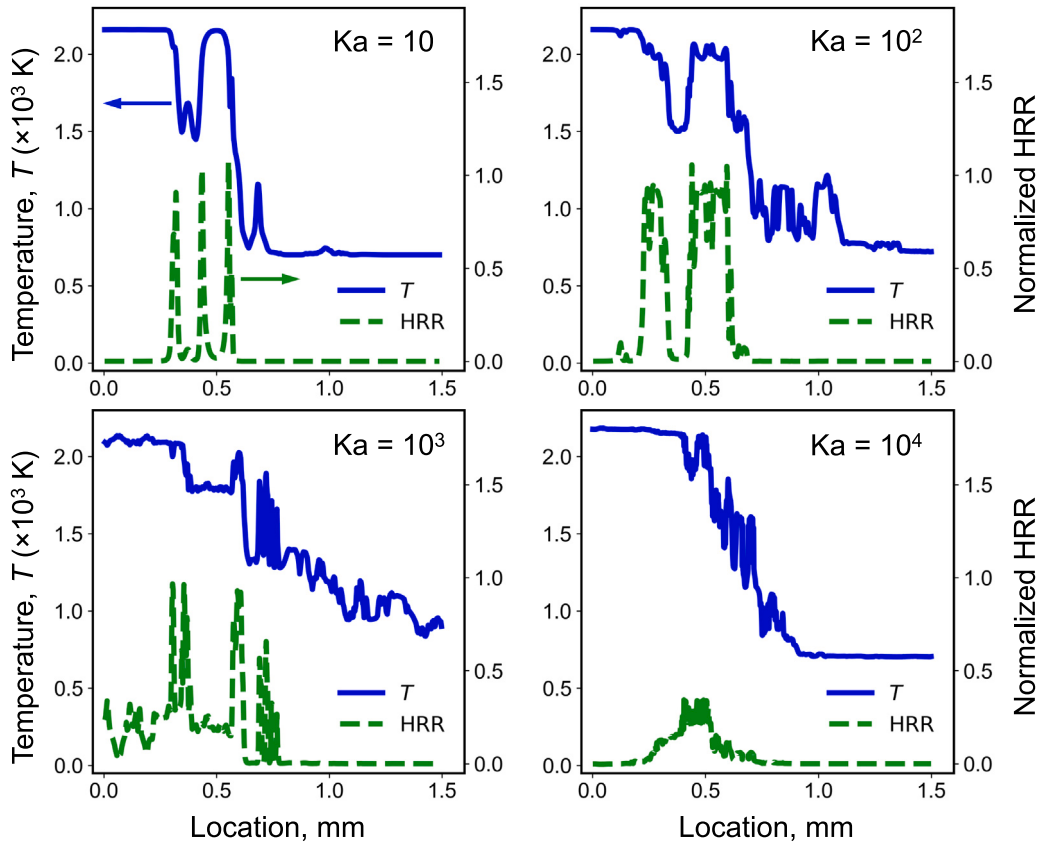


Fig. 5. Instantaneous streamwise profiles of temperature (blue, solid) and heat release rate (green, dash-dot) from the ODT calculations. The heat release rate is normalized by the laminar peak heat release rate (7.910×10^{14} erg/g s). Note that the origin of the horizontal axis does not coincide with the ODT inlet, and the flame propagates from right to left.

Species mass fractions from the ODT calculation, normalized by their respective peak values in the laminar flame, are shown in Fig. 6. Results closely follow the DNS observations for temperature and heat release rate. For $Ka = 10^2$ and 10^3 , mass fractions of the radical species fluctuate significantly. CH_2O is primarily associated with the pre-heat zone. We see that CH_2O is indeed primarily ahead of the reaction zone. For $Ka = 10^4$, the peak mass fractions of the radicals O, OH, H and HO_2 are lower, which agrees with the HRR reduction trend shown in Fig. 5a, indicating disruption and extinction of the flames inner layer.

6.2.3. Turbulent flame speed

Mean turbulent flame speed S_T is compared between the DNS and the ODT. The flame speed S_T^n of a given ODT simulation n is calculated based on the fuel consumption rate over the ODT domain L as [44]

$$S_T^n(t) = \frac{Y_u^{\text{CH}_4} - Y_b^{\text{CH}_4}}{\rho_u A_c} \int_0^L -\dot{\omega}_{\text{CH}_4}(t, x) dx, \quad (15)$$

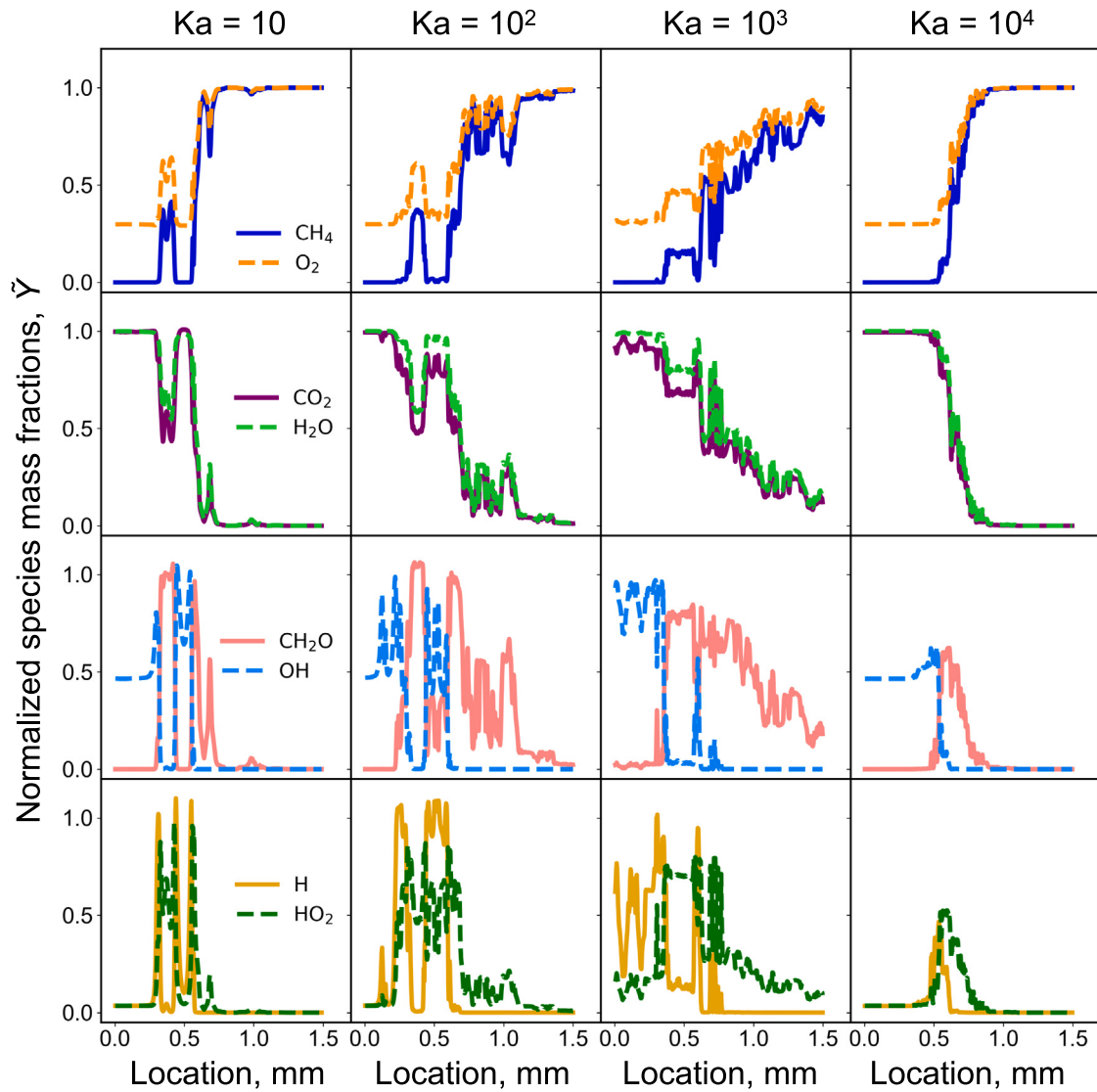


Fig. 6. Instantaneous streamwise profiles of the species mass fractions in the ODT calculations. Mass fractions are normalized by the respective peak values in the laminar flame. Note that the origin of the horizontal axis does not coincide with the ODT inlet, and the flame propagates from right to left.

where $Y_u^{\text{CH}_4}$ and $Y_b^{\text{CH}_4}$ are the methane mass fractions in the reactants and products, respectively, and $-\dot{\omega}_{\text{CH}_4}$ is the consumption rate of CH_4 .

ODT is a stochastic simulation. Therefore, we ensemble average S_T^n over N simulations to determine the mean turbulent flame speed $S_T(t)$ as

$$S_T(t) = \frac{1}{N} \sum_{n=1}^N S_T^n(t). \quad (16)$$

In the limit as $N \rightarrow \infty$, the ODT turbulent flame speed converges to a constant value once a steady state (with respect to time) is reached. All further results will show ODT data ensemble averaged over 80 realizations ($N = 80$).

In Fig. 7, the mean turbulent flame speed is shown as a function of time. As Ka increases from 10 to 10^2 and to 10^3 , the DNS mean turbulent flame speed increases from ≈ 100 cm/s to 200 cm/s and to 360 cm/s, respectively. We also see that with increasing Ka , the fluctuations in $S_T(t)$ increase as the result of increased turbulent mixing, and these fluctuations ultimately accelerate the overall flame propagation.

While $S_T(t)$ steadily increases from $Ka = 10$ to $Ka = 10^3$, at $Ka = 10^4$, $S_T(t)$ appears to be comparable to that at $Ka = 10^3$. We emphasize, however, that $S_T(t)$ cannot be compared directly between $Ka = 10^4$ and the lower speed cases since both the domain width and the turbulent

integral scale are four times smaller in the former case. Second, at $Ka = 10^4$, S_T gradually increases and no statistically stationary steady state is observed. This is due to the turbulent heating of the flow, which arises both as a result of the kinetic energy dissipation on small scales and a strong compressive component of the flow field present at high turbulent Mach numbers associated with $Ka = 10^4$ turbulence.

ODT reaches a steady state faster than DNS at $Ka = 10$ and 10^2 , while for $Ka = 10^3$ both DNS and ODT converge to a steady state after approximately one large-scale eddy turnover time. The S_T fluctuations (effectively, noise) in ODT are not related to the flame structure fluctuations. Rather they are related to the number of realizations used in the evaluation of S_T . Therefore, the amplitude and frequency of fluctuations of S_T in ODT should not be compared to those in DNS, which reflect inherent variability in the flame structure. Rather, the key quantity of comparison is the mean turbulent flame speed. For all Ka values considered, the ODT results are within 10% of the DNS. For $Ka = 10$ and 10^2 , ODT slightly underestimates the mean DNS turbulent flame speed, while for $Ka = 10^3$ it overestimates it. Interestingly, ODT is able to capture the dynamics even for $Ka = 10^4$ as it is able to reproduce both the overall turbulent flame speed and its increasing trend. Note that viscous heating is explicitly captured in ODT through the last term of Eq. (4), which as noted earlier is partially responsible for the gradual increase in S_T over time at $Ka = 10^4$.

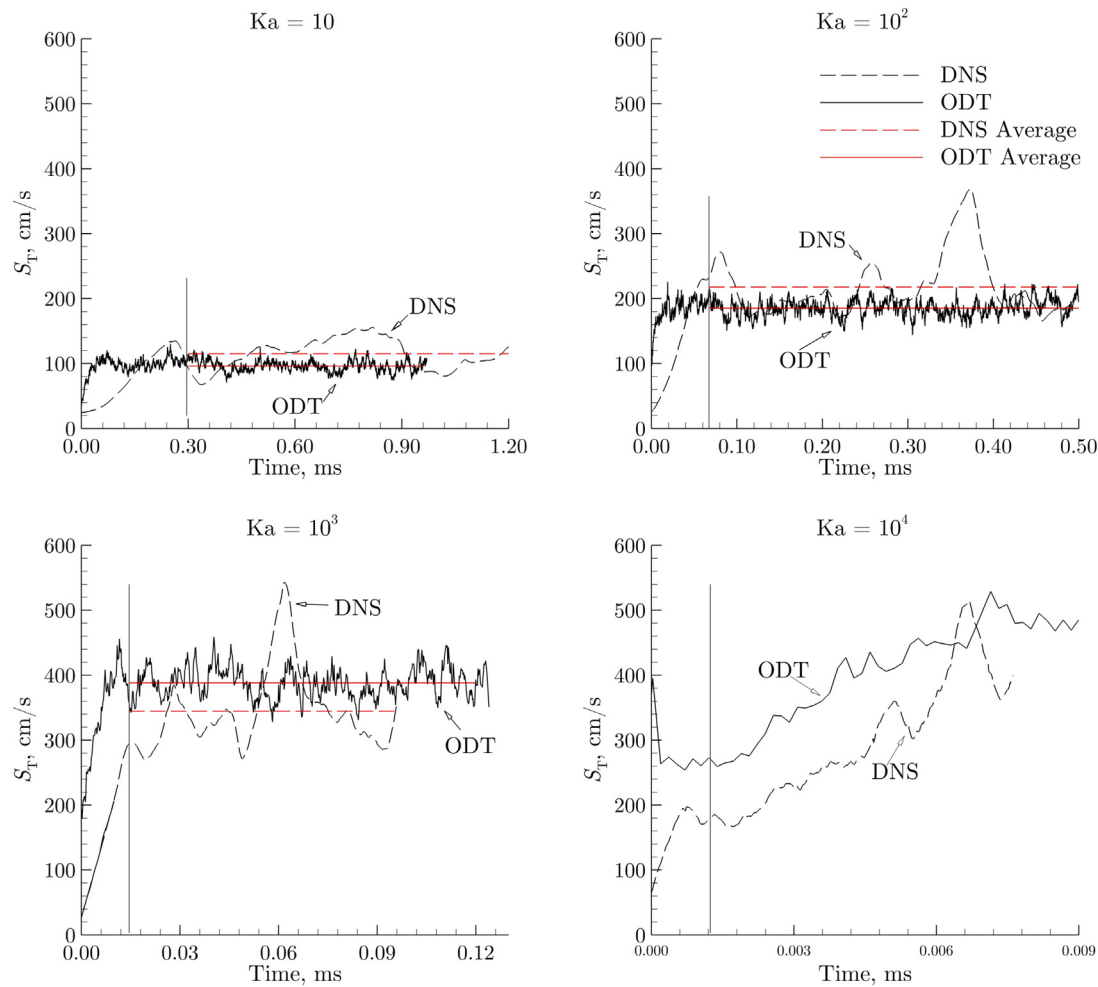


Fig. 7. Turbulent flame speed as a function of time in ODT (solid) and DNS (dashed). Red solid and dashed lines mark the average ODT and DNS values, respectively. The solid vertical line indicates one large-scale eddy turnover time.

6.2.4. Turbulent flame width

Mean turbulent flame width δ_T is compared between DNS and ODT. The δ_T is calculated in ODT in two steps. First, at each instant in time and space, methane mass fraction $\bar{Y}_{CH_4}^n(t, x)$ is ensemble averaged over N ODT realizations as

$$\bar{Y}_{CH_4}(t, x) = \frac{1}{N} \sum_{n=1}^N Y_{CH_4}^n(t, x). \quad (17)$$

As before, $N = 80$. Using $\bar{Y}_{CH_4}(t, x)$, δ_T is then measured as the distance between $x_L = \min(x)$ for which $\bar{Y}_{CH_4}(t, x_L) > 0.05 \cdot Y_b$ and $x_R = \max(x)$ for which $\bar{Y}_{CH_4}(t, x_R) < 0.95 \cdot Y_u$. This procedure is analogous to the flame width calculation in DNS, in which the CH_4 mass fraction is averaged over the planes normal to the mean direction of the flame [40]. Then, the flame width is calculated as that of ODT.

Fig. 8 shows the calculated δ_T in DNS and ODT. It can be seen that ODT is in qualitative agreement with DNS, and it captures the increase of δ_T with time and Ka . Quantitatively however, ODT overestimates the flame width when compared to DNS. Furthermore, for $Ka = 10^4$, both DNS and ODT results show much lower δ_T compared to $Ka = 10^3$. This is again a result of the smaller turbulent integral scale, as noted above. In ODT the quasi-steady state of the flame speed is less pronounced and is reached later in the simulation. This shows that in ODT, turbulent flame width converges more slowly to a steady state than the turbulent flame speed (Fig. 7), which reaches a steady state by the first large eddy turnover time. This difference could reflect the gradual extension of the trailing edge of the flame after the leading edge has converged to statistically steady propagation.

6.2.5. State space statistics

Temperature-conditioned statistics are often used to analyze the thermochemical state-space structure of turbulent flames because they reveal the effects of finite-rate kinetics, which cause the thermochemical state to deviate from equilibrium. To construct the joint probability density function (jPDF), data are collected over the entire domain starting from time equal to one large-scale eddy turnover time after the flame is initialized. This is done to ensure that the initial transient is excluded from consideration. Data are then taken at regular intervals until the end of the simulation. Each simulation is run for at least three large-scale eddy turnover times.

Figs. 9 and 10 show the jPDFs of the mass fractions of major species CH_4 and H_2O vs. temperature, comparing DNS (top panels) and ODT (bottom panels). Features of these plots are similar to those of other major species CO_2 and O_2 . As Ka is increased from 10 to 10^4 , the scatter for each case narrows, and the CH_4 mass fraction distribution rises above the laminar flame profiles, while H_2O values fall further below the laminar values. A notable feature of these jPDFs of CH_4 and H_2O , the mass fraction distributions of which vary monotonically through the flame, is the increased linearity with increasing Ka of the locus of the maximum-probability region. The thermochemical state-space structure is determined by the collective action of chemical reactions, which alter the chemical composition locally, and transport processes, both molecular and turbulent, which redistribute species and enthalpy. As Ka increases, turbulent mixing progressively dominates molecular thermal and diffusion transport, which asymptotically brings the system to an effective $Le = 1$ regime, when all species are transported uniformly

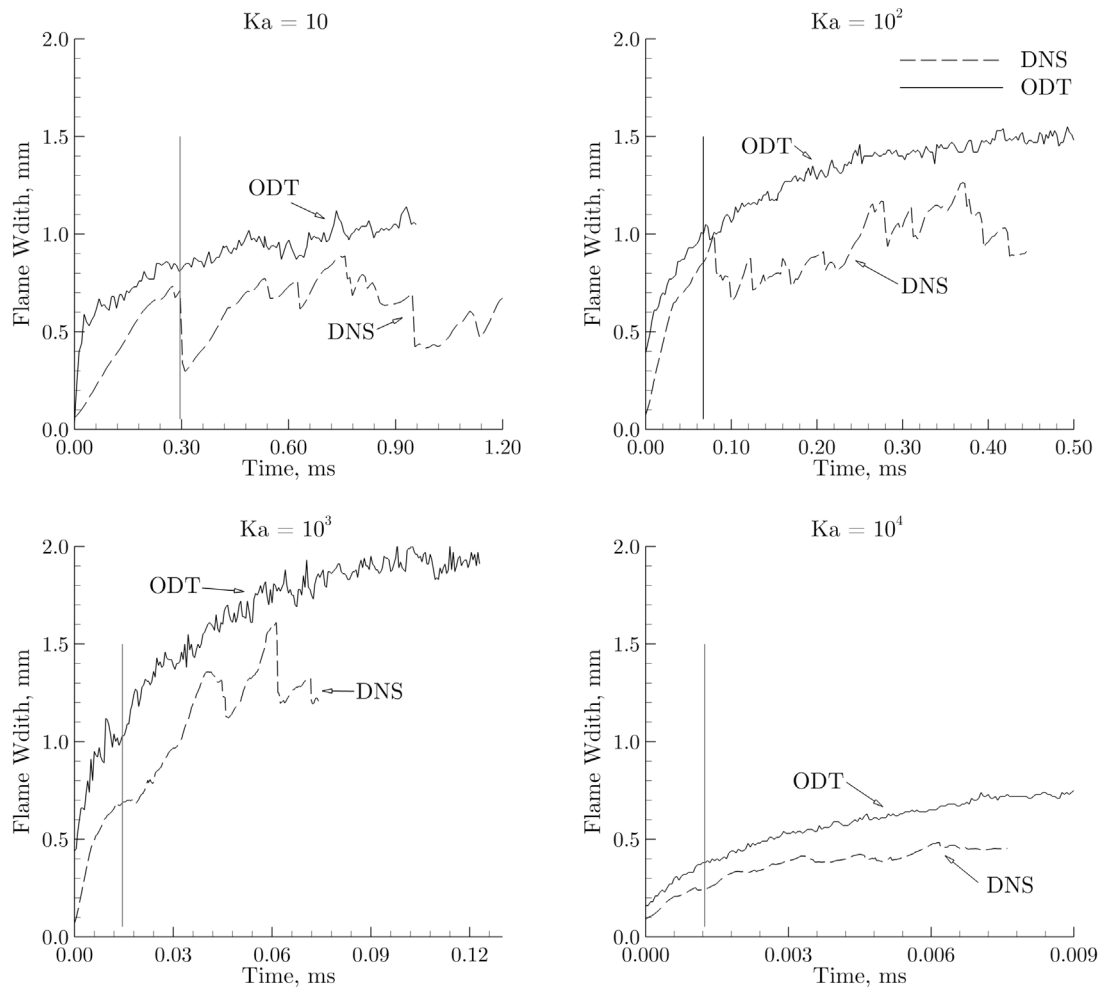


Fig. 8. Turbulent flame width as a function of time for ODT (solid) and DNS (dashed). The solid vertical line denotes one large-scale eddy turnover time.

by turbulence. This same change in the jPDFs has been previously observed in DNS studies of high-speed CH₄ and H₂ flames by Aspden et al. [65,67].

The DNS and ODT results for \tilde{Y}_{CH_4} and $\tilde{Y}_{\text{H}_2\text{O}}$ are in agreement for all Ka values tested. The closest agreement is for Ka = 10⁴, which is consistent with the proposed physical interpretation that at Ka = 10⁴ the overall flow structure is governed primarily by passive turbulent mixing, rather than by configurational effects of the flame associated with the interplay of turbulent folding and local flame propagation. This excellent agreement at Ka = 10⁴ is not universal and is limited to \tilde{Y}_{CH_4} and $\tilde{Y}_{\text{H}_2\text{O}}$.

In Figs. 11 and 12, jPDFs for CH₂O and OH are compared between DNS and ODT. Overall, ODT captures the trends exhibited in the DNS, and close agreement is observed in the highest probability regions (colored as dark orange). Differences are primarily in the lower probability regions (colored as light yellow). Again, the agreement between DNS and ODT appears to decrease with increasing Karlovitz number. Fig. 11 shows that as Ka increases, the CH₂O distribution gradually shifts to a higher temperature. Such a shift away from the laminar-flame profile is caused by the dissipative turbulent heating of the flow. Finally, for Ka = 10, ODT predicts a somewhat broader mass-fraction distribution near 1500 K compared to DNS, which extends both above and below the laminar-flame curve.

The production of OH coincides with the heat release as can be seen by comparing Fig. 12 with Fig. 13. Comparison of the OH jPDFs in DNS and ODT shows good agreement at Ka = 10² and 10³. For Ka = 10, however, ODT shows extended distribution below the laminar-flame

curve, which is not observed in DNS. At Ka = 10⁴, ODT captures the trend of jPDFs moving toward higher temperatures in agreement with DNS, however peak values of the OH mass fraction are higher in ODT than in DNS.

Lastly, we compare the heat release rates between DNS and ODT (Fig. 13). For Ka = 10, moderately good agreement between DNS and ODT is observed. Most notably, lower HRR are observed in ODT at high temperatures. Specifically, between 1700 to 2000 K, ODT shows significantly more heat release below the laminar-flame curve compared to DNS, though the probability of such low-HRR events is relatively low. This difference can also be seen for Ka = 10². At Ka = 10³, good agreement is observed for the entire jPDF. At Ka = 10⁴, ODT significantly overpredicts the heat release rate.

6.2.6. ODT prediction at a larger integral length scale for Ka = 10⁴

As noted earlier, the DNS at Ka = 10⁴ was carried out at an integral length scale of 0.04 mm, which is smaller than 0.158 mm used in the simulations for Ka = 10 – 10³. Also as was discussed in Section 6.1, extrapolation of the DNS flame speed at Ka = 10⁴ to a four times larger domain would predict a significant increase in S_T compared to smaller Ka values (Fig. 3). Here we discuss whether such prediction is indeed supported by the ODT. For this purpose, an ODT simulation was performed at Ka = 10⁴ with a larger integral scale of $L_{11} = 0.158$ mm equal to that used in the ODT and DNS simulations at lower Ka. This case is referred to as Ka = 10⁴-Large L_{11} (Table 2), and its turbulent flame speed and flame width are shown in Fig. 14.

Indeed, in agreement with the prediction discussed in Section 6.1, at Ka = 10⁴, S_T breaks the overall trend of a slower growth with Ka as it

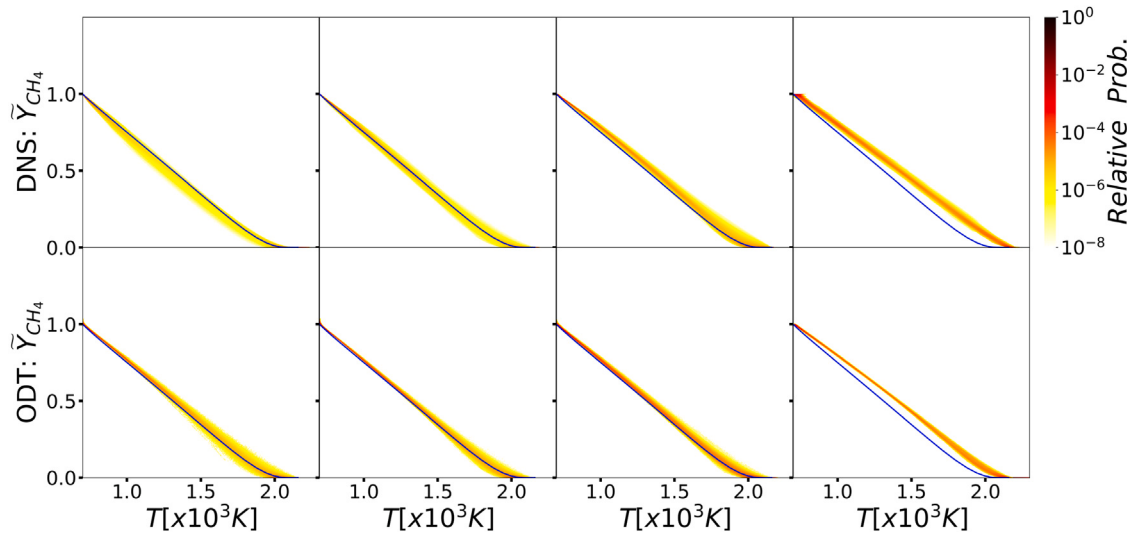


Fig. 9. DNS and ODT jPDFs of the normalized CH_4 mass fraction and temperature. The blue line shows the laminar flame solution for reference. Mass fractions are normalized by the peak laminar-flame mass fraction. From left to right: $\text{Ka} = 10, 10^2, 10^3, 10^4$.

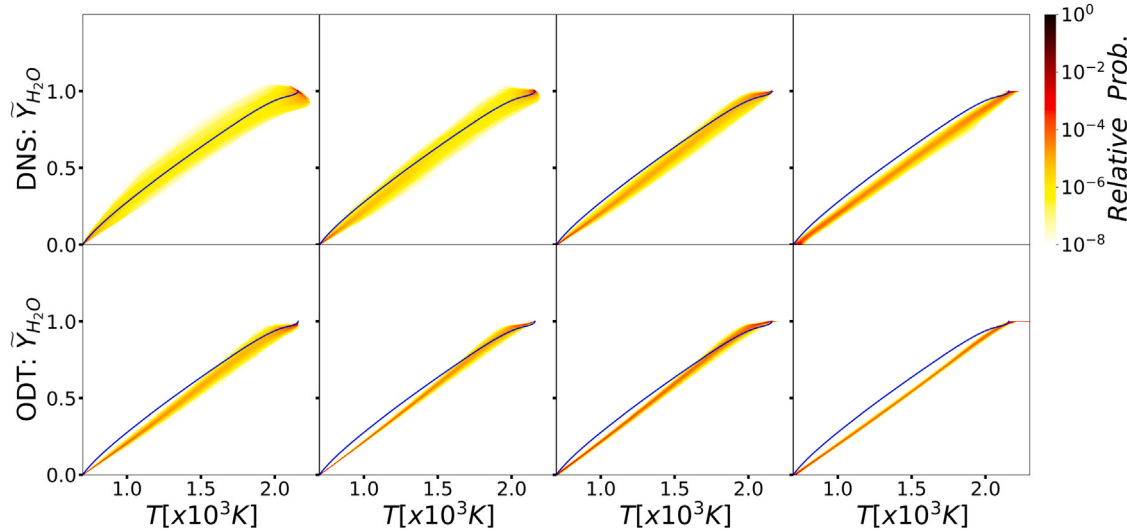


Fig. 10. DNS and ODT jPDFs of the normalized H_2O mass fraction and temperature. The blue line shows the laminar flame solution for reference. Mass fractions are normalized by the peak laminar-flame mass fraction. From left to right: $\text{Ka} = 10, 10^2, 10^3$, and 10^4 .

significantly increases from $\text{Ka} = 10^3$ to 10^4 . This is in contrast with the classical bending phenomenon observed in experimental measurements of S_T [62,63], though it is important to note that none of the prior turbulent combustion experiments have achieved such high values of Ka . Furthermore, this finding agrees with the prior DNS results by Aspden et al. [59]. This issue requires further investigation in the context of turbulence-chemistry coupling. Finally, Fig. 15 shows that the jPDFs of the mass fractions of CH_4 , CH_2O , as well as HRR vs. temperature are wider for the larger integral scale or correspondingly higher turbulent Reynolds number. While the ODT model can capture the expected trend in S_T at $\text{Ka} = 10^4$ we would expect the same discrepancies between the ODT and the DNS in the jPDFs that we saw in the smaller domain comparison because of limitations of the ODT model.

6.2.7. ODT performance at $\text{Ka} = 10^4$

For the lower Ka values, the flame structure is relatively close to the flamelet limit, for which a locally one-dimensional representation as instantiated in the ODT model formulation is relatively accurate. With increasing Ka , multi-dimensional effects become stronger, accounting

for the decreasing agreement of ODT with DNS. It is clear that ODT is not able to serve as a DNS surrogate at extreme Karlovitz numbers like $\text{Ka} = 10^4$. This is a fundamental limitation of the ODT model because of its limited ability to capture compressible thermodynamics.

An additional consideration is that the domain size for $\text{Ka} = 10^4$ is smaller than for the lower Ka values, indicated in Table 1. DNS with laterally periodic boundary conditions is subject to some attendant degree of organization of the vorticity structure. This is accentuated by thermal expansion effects, because dilatation is roughly isotropic locally but must be redirected by the boundary conditions through the non-local influence of the pressure field so that all net volume production is streamwise oriented. The resulting finite-domain effect increases with decreasing domain size. This is consistent with the marked differences between the DNS results for $\text{Ka} = 10^4$ and the trends indicated by the relatively mild Ka sensitivity of the DNS results for lower Ka values. In ODT, all dilatation is streamwise oriented by construction, so it is not subject to the dilatation-enhanced domain-size sensitivity of the DNS cases. This is illustrated by the relatively mild differences between the ODT CH_2O (Fig. 11, lower right) and HRR (Fig. 13, lower right) $\text{Ka} = 10^4$ results for the small integral

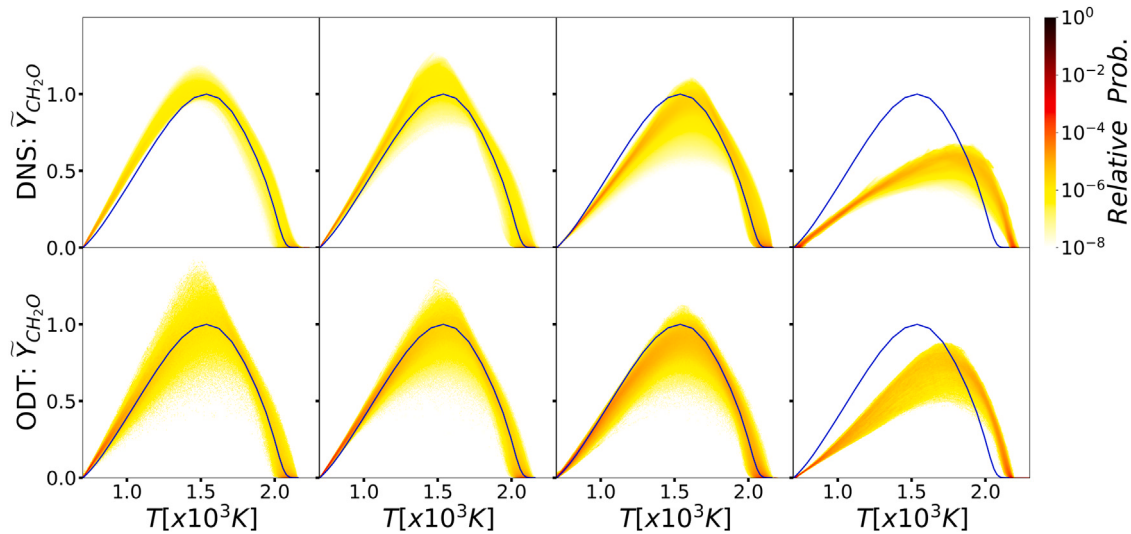


Fig. 11. DNS and ODT jPDFs of the normalized CH_2O mass fraction and temperature. The blue line shows the laminar flame solution for reference. Mass fractions are normalized by the peak laminar-flame mass fraction. From left to right: $\text{Ka} = 10, 10^2, 10^3$, and 10^4 .

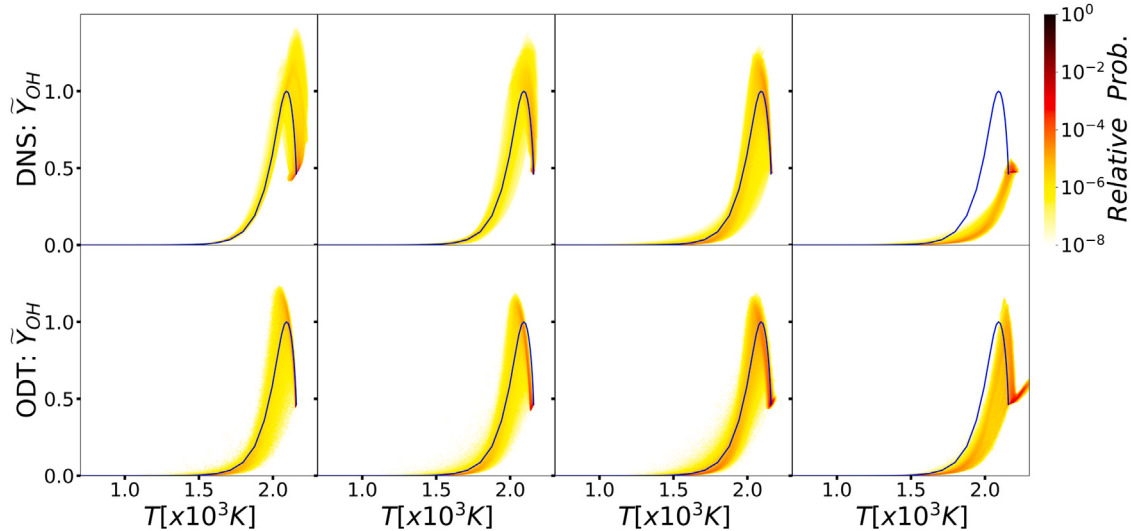


Fig. 12. DNS and ODT jPDFs of the normalized OH mass fraction and temperature. The blue line shows the laminar flame solution for reference. Mass fractions are normalized by the peak laminar-flame values. From left to right: $\text{Ka} = 10, 10^2, 10^3$, and 10^4 .

scale and their counterparts for the large integral scale (Fig. 15), where the integral scale is the ODT-accessible representation of the domain-size effect. The DNS domain-size sensitivity cannot be investigated for $\text{Ka} = 10^4$ owing to the high computational cost of running a large-domain case for this Ka value, but in the future, a small-domain DNS run will be performed for $\text{Ka} = 10^3$ to assess the domain-size sensitivity for a Ka value of interest.

7. Concluding remarks

Freely propagating turbulent methane-air flames (unburned mixture temperature of 700 K, pressure of 30 atm, and equivalence ratio of 0.7) were modeled over a wide range of turbulence intensities with the objective of assessing the accuracy of the one-dimensional turbulence (ODT) model against the 3D DNS data. This is the first attempt ever made to analyze the performance of a stand-alone turbulent combustion model across such a wide range of combustion regimes from wrinkled flames to broken reaction zones, thus providing a comprehensive assessment of the model performance. Instantaneous temperature and

species profiles, turbulent flame speed and width, and jPDFs of species mass fractions and heat release rate vs. temperature are presented and compared for ODT and DNS at Karlovitz numbers of 10, 10^2 , 10^3 , and 10^4 . These computed responses are used to assess the accuracy of the ODT model.

Overall, ODT is found to be in close agreement with the DNS up to $\text{Ka} = 10^3$. Specifically, trends in the DNS data as a function of Ka are captured by the ODT rather well. Qualitatively, ODT shows the key flame characteristics, including the instantaneous temperature and heat release rate distributions, similar to DNS at each Karlovitz number tested. ODT also captures global flame characteristics, including the turbulent flame speed and flame width, in agreement with DNS. It is encouraging that the mean turbulent flame speed as determined by ODT is within 10% of the values in DNS at each Karlovitz number. At a detailed level, jPDFs of major and minor species and temperature are generally well reproduced by the ODT when compared to those computed in DNS. The best agreement between DNS and ODT is observed at $\text{Ka} = 10^3$ while the worst agreement is at $\text{Ka} = 10^4$ due to the limitations in the ODT model. At all Ka values tested, jPDFs of the

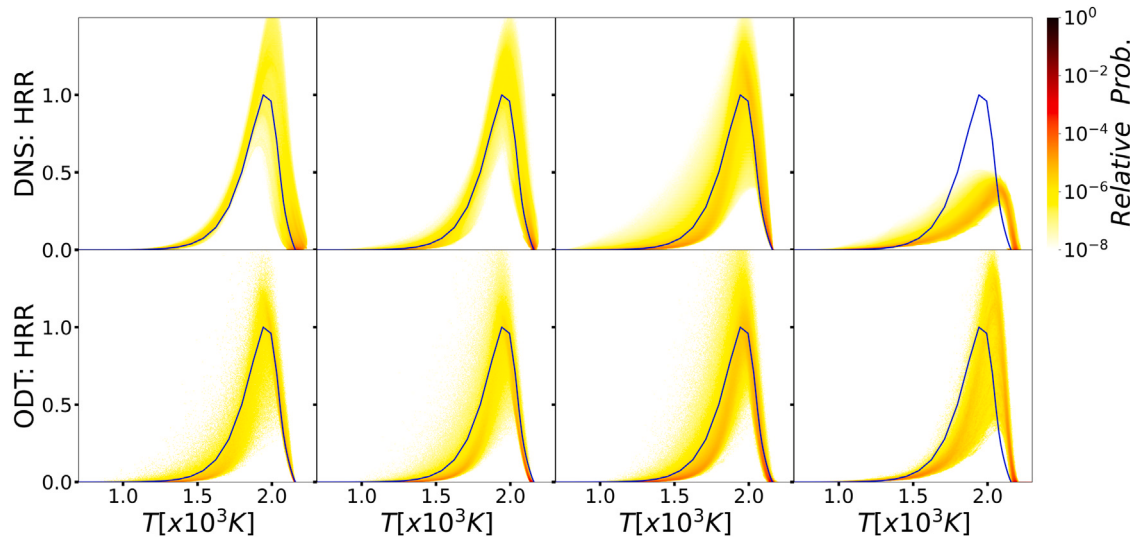


Fig. 13. DNS and ODT jPDFs of the normalized heat release rate and temperature. The blue line shows the laminar flame solution for reference. The heat release rate is normalized by the peak laminar-flame value. From left to right: $K_a = 10, 10^2, 10^3$, and 10^4 .

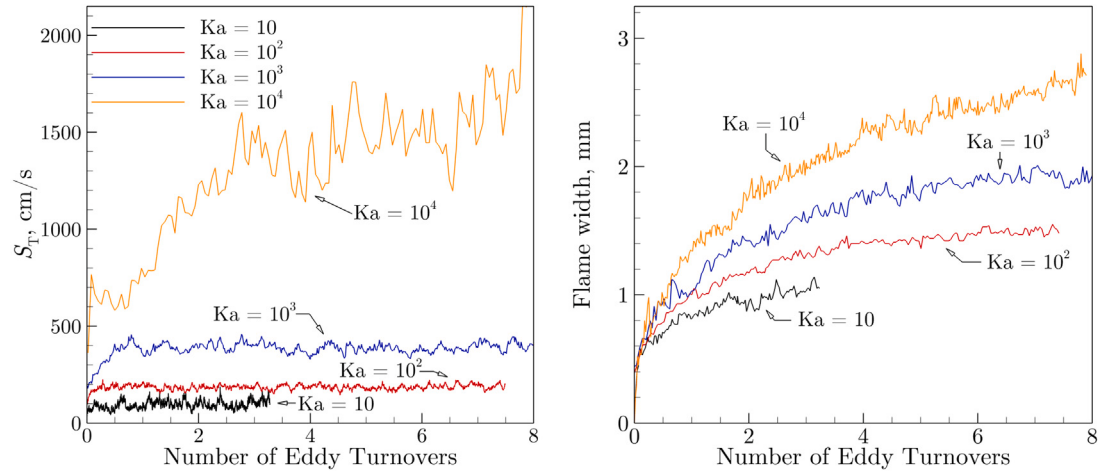


Fig. 14. ODT turbulent flame speed (top) and flame width (bottom) as a function of time normalized by the large-scale eddy turnover times, all computed with $L_{11} = 0.158$ mm.

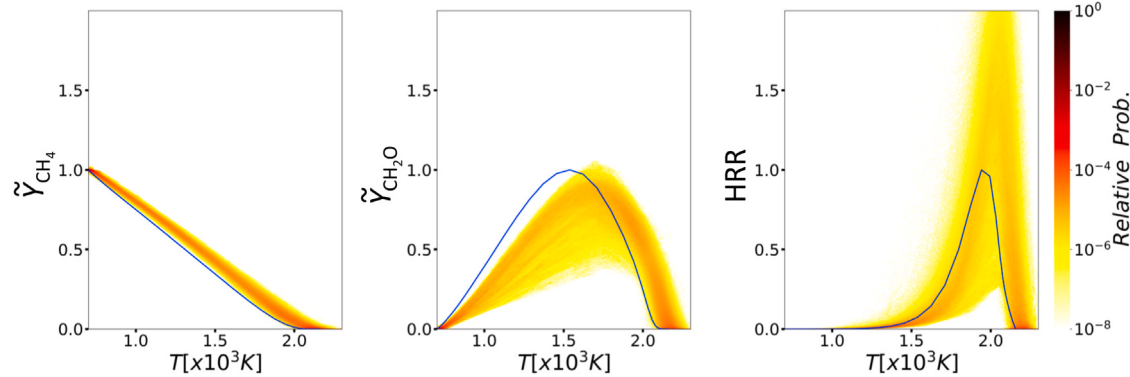


Fig. 15. ODT jPDFs of the normalized mass fractions of CH_4 , CH_2O , as well as the normalized heat release rate vs. temperature for $K_a = 10^4$ with $L_{11} = 0.158$ mm. The blue line shows the corresponding laminar-flame solution.

major and minor species vs. temperature agree well, except for the low-probability regions, and the difference is most pronounced for minor species at $K_a = 10$, where ODT also produced a smaller scatter in the jPDF than DNS.

The current effort demonstrates the promise of ODT as a DNS surrogate for the reaction model reduction as well as the sensitivity analysis of the turbulent flame structure and properties with respect to chemistry. To this end, the use of ODT for chemical mechanism

reduction is discussed in a companion paper as Part II [13], while the use of ODT for chemistry sensitivity analysis is forthcoming.

CRediT authorship contribution statement

Zoltan Jozefik: Obtained and analyzed the ODT results, Manuscript preparation and revision. **Matthew E. Harvazinski:** Obtained and analyzed the ODT results, Manuscript preparation and revision. **Venkateswaran Sankaran:** Obtained and analyzed the ODT results, Manuscript preparation and revision. **Sai Sandeep Dammati:** Obtained and analyzed the DNS results, Manuscript preparation and revision. **Alexei Y. Poludnenko:** Obtained and analyzed the DNS results, Manuscript preparation and revision. **Tianfeng Lu:** Developed the 21-species skeletal model, Manuscript preparation and revision. **Alan R. Kerstein:** Contributed to the ODT formulation, Analysis of results, Manuscript preparation and revision. **Rui Xu:** Analyzed results, Manuscript preparation and revision. **Hai Wang:** Analyzed results, Manuscript preparation and revision.

Declaration of competing interest

The authors declare that they have no known competing financial interests or personal relationships that could have appeared to influence the work reported in this paper.

Acknowledgments

Distribution Statement A. Approved for public release: distribution is unlimited AFRL-2022-2479. This material is based upon work supported by the Air Force Office of Scientific Research (AFOSR), USA under award number 19RQCOR100 and 22 RQCOR003. SSD and AYP acknowledge funding support from AFOSR, USA under Grant FA9550-21-1-0012. HW acknowledges funding supports from AFOSR, USA under Grant FA9550-20-1-0398, and from ONR, USA under Grant N00014-21-1-2475. Any opinions, findings, and conclusions or recommendations expressed in this material are those of the author(s) and do not necessarily reflect the views of the United States Air Force, the Department of Defense, or the U.S. government.

Appendix A. ODT turbulence model

ODT models turbulent motions, which accelerate mixing, as a series of stochastic rearrangement events. These 'eddy events' may be interpreted as the model analog of the individual turbulent eddies. When an eddy event takes place, it interrupts the time advancement of other processes. In Eqs. (1)–(4), EE symbolically denotes occurrences of these instantaneous events. During each eddy event, an instantaneous transformation is applied to the property profiles over a chosen spatial interval $[x_0, x_0 + l_e]$, where x_0 represents the eddy starting location and l_e is the eddy length. The complete definition of the model involves specification of the transformation, as well as the procedure for selecting the parameters x_0 and l_e and the time sequence of events. The selection procedure is governed by a random process. Hence, ODT is a stochastic modeling method, which generates ensembles of simulated realizations, from which statistical observables can be extracted. The ODT implementation used in this study was described in detail in [29].

A.1. Eddy events

An eddy event models the effects of a 3D eddy using a 1D rearrangement. Eddy events are qualitatively similar to turbulence in that they have the effect of increasing gradients by redistributing the fluid elements along the 1D domain. Each eddy event consists of two mathematical operations. One is a triplet map representing fluid displacements associated with a notional turbulent eddy, and the other one is a kernel operation. The functional form chosen for the triplet

map is the simplest of a class of mappings that satisfy the physical requirements of measure preservation, continuity, and scale locality over the eddy interval. The triplet map is conveniently represented by its inverse $f(x)$, such that the map moves fluid at location $f(x)$ to location x , where $f(x)$ is of the form described in [68] and written as

$$f(x; x_0, l_e) \equiv x_0 + \begin{cases} 3(x - x_0) & \text{if } x_0 \leq x \leq x_0 + \frac{1}{3}l_e, \\ 2l_e - 3(x - x_0) & \text{if } x_0 + \frac{1}{3}l_e \leq x \leq x_0 + \frac{2}{3}l_e, \\ 3(x - x_0) - 2l_e & \text{if } x_0 + \frac{2}{3}l_e \leq x \leq x_0 + l_e, \\ x - x_0 & \text{otherwise.} \end{cases} \quad (\text{A.1})$$

This mapping takes a line segment $[x_0, x_0 + l_e]$, shrinks it to a third of its original length, and then places three copies of it on the original domain. The middle copy is reversed, which ensures that property fields remain continuous and introduces the rotational folding effect of an eddy motion. All quantities outside the interval $[x_0, x_0 + l_e]$ are unaffected. The triplet map function conserves all quantities, increases scalar gradients and decreases length scales, which reflects the behavior of the notional turbulent eddies [69]. In Fig. A.16, the triplet map is visually shown for a notional linear increase of an arbitrary quantity ϕ along x . The triplet map instantaneously rearranges fluid elements as depicted.

For a constant-density flow, the triplet map is followed by the addition to each velocity component of a kernel function $K(x)$, defined as the fluid displacement profile $x - f(x)$ times a component-dependent coefficient. This implements pressure-induced energy redistribution among velocity components while maintaining conservation of energy and momentum. The redistribution of energy among velocity components emulates the tendency of turbulent eddies to drive the flow toward isotropy. The generalization of this procedure to variable-density flows is explained in [19]. $K(x)$ encapsulates the map-induced transport and thereby is central to various aspects of the mathematical formulation of the model, including several specific aspects that are discussed below.

A.2. Eddy rate distribution

The ODT velocity profiles evolve through the specification of the occurrences of eddy events. Conversely, the velocity profile supplies information that determines the size, location, and frequency of these events. The eddy selection process is stochastic and follows the variable density formulation of Ashurst and Kerstein [19,70].

As in the dimensional relationships applied to fully developed turbulence, a relationship can be formulated between the size of a given eddy event, its associated energy, and a time scale denoted τ . The value of τ associated with a given interval $[x_0, x_0 + l_e]$ of a possible eddy occurrence at a given instant is expressed as

$$\frac{1}{\tau} = C \sqrt{\frac{2K_0}{\rho_0 l^3} (E_{\text{kin}} - Z E_{\text{vp}} - E_{\text{pe}})}, \quad (\text{A.2})$$

where $\rho_0 = \int \rho K^2(x) dx$, and $K_0 = \int K^2(x) dx$. E_{vp} is a viscous penalty defined dimensionally as $E_{\text{vp}} = \frac{1}{2} \bar{\mu}^2 / \bar{\rho}$, where $\bar{\rho}$ and $\bar{\mu}$ are the average density and harmonically averaged [24] dynamic viscosity in the eddy region. The input model parameter C scales the eddy event frequency, and thereby the turbulence intensity. The input model parameter Z is a viscous penalty factor, which controls the suppression of nonphysically small eddies.

E_{kin} and E_{pe} are the kinetic and potential energy, respectively, which jointly determine the net kinetic energy available in $[x_0, x_0 + l_e]$ to drive an eddy turnover, as explained in [19] for variable density flows. In the present context, E_{pe} is the equivalent eddy-induced potential-energy change resulting from the acceleration of the variable density fluid caused by thermal expansion across a burning front. The expression $E_{\text{pe}} = \frac{8}{27} \int a(x) K(x) (\rho(f(x)) - \bar{\rho}) dx$ is derived in [71]. Here,

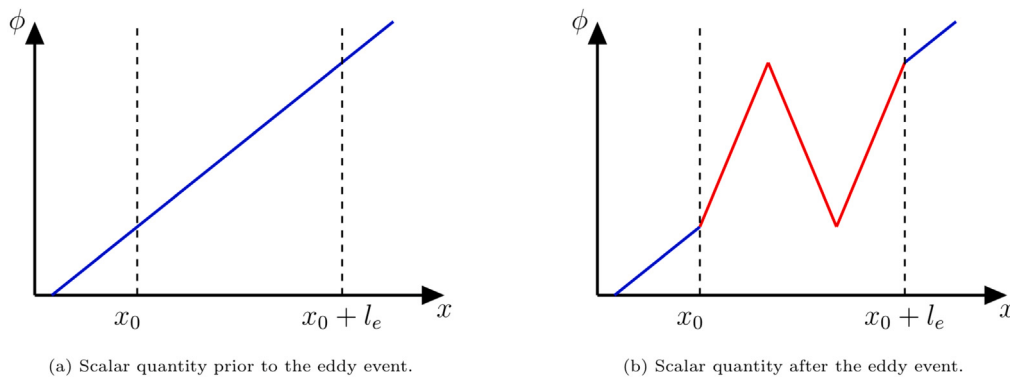


Fig. A.16. Action of a triplet map on a quantity ϕ . Left: ϕ increases linearly along x . Right: ϕ profile along x after the application of a triplet map. Distribution of ϕ outside the $[x_0, x_0 + l_e]$ interval is unaffected.

$a(x)$ is the Lagrangian time rate of change of the advecting velocity $u_1(x)$ during the time advancement between eddy events. This potential energy change is nonzero only if the density varies within $[x_0, x_0 + l_e]$, just as vertical rearrangements in a flow subject to gravitation induce potential-energy changes only if the density varies spatially. Additional discussion of E_{pe} , which in this context idealizes the Darrieus-Landau instability, is provided in [29].

Apart from model-specific details of the evaluation of quantities on the right-hand side of Eq. (A.2), the expression is a conventional estimate of the local eddy turnover time. In ODT, eddy implementation is instantaneous, and in this context τ is a time scale governing the event occurrence frequency. The evaluation of τ depends on the instantaneous flow state in $[x_0, x_0 + l_e]$, so eddy occurrences are responsive to the unsteadiness resulting from transients or statistical fluctuations inherent in the time-advancement process. The eddy occurrences thus depend on the effects of prior eddies and affect future eddy occurrences. These dependencies induce spatio-temporal correlations among eddy events, leading to a physically based representation of turbulence intermittency.

On this basis, the rate of eddy occurrences is specified. An eddy rate distribution λ_e is defined by the relation $\lambda_e(x_0, l_e) dx_0 dl_e = (1/l_e^2 \tau(x_0, l_e)) dx_0 dl_e$. Both the left- and right-hand sides of this equation have dimensions of frequency to characterize eddy occurrences in a fixed $dx_0 dl_e$ sub-region of the set of all possible eddies. The total rate of all eddies is $\Lambda = \iint \lambda_e(x_0, l_e) dx_0 dl_e$. Eddy occurrence times are governed by the Poisson statistics with a mean rate Λ , bearing in mind that Λ as well as $\lambda_e(x_0, l_e)$ are time-varying. Hence, the PDF of the time between successive occurrences $P(\Delta t)$ is given by $P(\Delta t) = \Lambda e^{(-\Lambda \Delta t)}$. For efficiency purposes, this is implemented by oversampling and thinning of the Poisson process with an acceptance-rejection method. For further details see [19,72].

Details of the oversampling procedure are immaterial because the thinning step enforces eddy sampling based on the current eddy rate distribution $\lambda_e(x_0, l_e)$. The left eddy boundary x_0 is sampled uniformly within the 1D domain. The eddy length l is sampled from a PDF with a convenient physically motivated functional form parameterized by the fixed inputs, which include minimum l_{min} , most probable l_p , and maximum l_{max} eddy lengths. The minimum eddy length l_{min} allowed is set to an arbitrarily small value such that it does not restrict eddy size selection. To restrict the occurrence of unphysically large eddies, the maximum allowed eddy length l_{max} is a configuration-specific input. The most probable eddy length l_p is chosen to reflect the turbulent cascade property that the smallest eddies are most frequent within the inertial range. As noted, these considerations have no bearing on the outcome of the simulation and are governed solely by the goal to avoid excessive oversampling in order to optimize code efficiency.

Appendix B. Forcing model

Stationary forced homogeneous isotropic turbulence is generated on the ODT 1D domain with the strategy of keeping the turbulent kinetic energy (TKE) constant in the system. The ODT implementation was developed by Fistler et al. [61] and is adopted for the current simulations. Briefly, the TKE in the system is kept constant by performing, on average, one TKE injection ΔTKE per time interval $1/\lambda_{ke}$, where λ_{ke} is the mean occurrence rate of the TKE injection defined as

$$\frac{1}{\lambda_{ke}} = \frac{T_{inj} L_{inj}}{L}. \quad (\text{B.1})$$

Here T_{inj} is the injection eddy turnover time, L_{inj} is the injection length scale, and L is the domain length. This ensures that any given location in the ODT domain experiences on average one TKE injection once per injection eddy turnover time, consistent with the phenomenology of large-scale forcing. Akin to DNS forcing schemes [40,73,74], the TKE production rate P as well as the injection length scale L_{inj} and time scale T_{inj} of the forcing are required inputs. To match the energy production rate P at any given location, the average TKE increment ΔTKE that is required is given by

$$\Delta TKE = \frac{PLA_c}{\lambda_{ke}}. \quad (\text{B.2})$$

Here L is the domain length, A_c is the nominal cross-sectional area of the ODT domain, which is introduced to allow P to be expressed on a volumetric basis as required for this variable-density application, but A_c cancels out of all expressions after the forcing scheme is specified consistently.

Each TKE injection is applied within a chosen size interval, L_{inj} , of the domain. Application of the kernel $K(x)$, described in Appendix A.1, within a chosen event interval can change the TKE of any velocity component in that interval by any desired amount without changing the total momentum in that interval. For this variable-density case, if only the K kernel were used, then the total momentum would not be left unchanged. An injection event increases the total TKE of each velocity component by an amount $\frac{1}{3} \Delta TKE$.

Appendix C. Supplementary data

Supplementary material related to this article can be found online at <https://doi.org/10.1016/j.combustflame.2024.113379>.

References

- [1] A.M. Steinberg, P.E. Hamlington, X. Zhao, Structure and dynamics of highly turbulent premixed combustion, *Prog. Energy Combust. Sci.* 85 (2021) 100900.
- [2] A. Giusti, E. Mastorakos, Turbulent combustion modelling and experiments: Recent trends and developments, *Flow Turbul. Combust.* 103 (2019) 847–869.

- [3] J.H. Chen, Petascale direct numerical simulation of turbulent combustion—fundamental insights towards predictive models, *Proc. Combust. Inst.* 33 (2011) 99–123.
- [4] S.B. Pope, Small scales, many species and the manifold challenges of turbulent combustion, *Proc. Combust. Inst.* 34 (2013) 1–31.
- [5] T. Lu, C.K. Law, Toward accommodating realistic fuel chemistry in large-scale computations, *Prog. Energy Combust. Sci.* 35 (2009) 192–215.
- [6] J. Chen, Development of reduced mechanisms for numerical modelling of turbulent combustion, in: Workshop on Numerical Aspects of Reduction in Chemical Kinetics, CERMICS-ENPC Cite Descartes Champs-sur-Marne, France, 1997.
- [7] H. Wang, M. Frenklach, Detailed reduction of reaction mechanisms for flame modeling, *Combust. Flame* 87 (1991) 365–370.
- [8] C.K. Law, C.J. Sung, H. Wang, T. Lu, Development of comprehensive detailed and reduced reaction mechanisms for combustion modeling, *AIAA J.* 41 (2003) 1629–1646.
- [9] T. Lu, C.K. Law, A directed relation graph method for mechanism reduction, *Proc. Combust. Inst.* 30 (2005) 1333–1341.
- [10] J.F. Driscoll, J.H. Chen, A.W. Skiba, C.D. Carter, E.R. Hawkes, H. Wang, Premixed flames subjected to extreme turbulence: Some questions and recent answers, *Prog. Energy Combust. Sci.* 76 (2020) 100802.
- [11] P.E. Hamlington, R. Darragh, C.A. Briner, C.A. Towery, B.D. Taylor, A.Y. Poludnenko, Lagrangian analysis of high-speed turbulent premixed reacting flows: Thermochemical trajectories in hydrogen-air flames, *Combust. Flame* 186 (2017) 193–207.
- [12] X. Zhao, Y. Tao, T. Lu, H. Wang, Sensitivities of direct numerical simulations to chemical kinetic uncertainties: Spherical flame kernel evolution of a real jet fuel, *Combust. Flame* 209 (2019) 117–132.
- [13] R. Xu, S.S. Dammati, X. Shi, E.S. Genter, Z. Jozefik, M.E. Harvazinski, T. Lu, A.Y. Poludnenko, V. Sankaran, A.R. Kerstein, H. Wang, Modeling of high-speed methane-air turbulent combustion - Part II: Reduced methane oxidation chemistry, *Combust. Flame* (2024) 113380, <http://dx.doi.org/10.1016/j.combustflame.2024.113380>.
- [14] S.B. Pope, PDF methods for turbulent reactive flows, *Prog. Energy Combust. Sci.* 11 (1985) 119–192.
- [15] N. Peters, *Turbulent Combustion*, Cambridge University Press, Cambridge, U.K., 2001.
- [16] R.O. Fox, *Computational Models for Turbulent Reacting Flows*, Cambridge University Press, Cambridge, U.K., 2003.
- [17] E.D. Gonzalez-Juez, A.R. Kerstein, R. Ranjan, S. Menon, Advances and challenges in modeling high-speed turbulent combustion in propulsion systems, *Prog. Energy Combust. Sci.* 60 (2017) 26–67.
- [18] A.R. Kerstein, One-dimensional turbulence: Model formulation and application to homogeneous turbulence, shear flows, and buoyant stratified flows, *J. Fluid Mech.* 392 (1999) 277–334.
- [19] W.T. Ashurst, A.R. Kerstein, One-dimensional turbulence: Variable-density formulation and application to mixing layers, *Phys. Fluids* 17 (2005) 025107.
- [20] A.R. Kerstein, W.T. Ashurst, S. Wunsch, V. Nilsen, One-dimensional turbulence: Vector formulation and application to free shear flows, *J. Fluid Mech.* 447 (2001) 85–109.
- [21] R.C. Schmidt, A.R. Kerstein, S. Wunsch, V. Nilsen, Near-wall LES closure based on one-dimensional turbulence modeling, *J. Comput. Phys.* 186 (2003) 317–355.
- [22] R.C. Schmidt, A.R. Kerstein, R. McDermott, ODTLES: A multi-scale model for 3D turbulent flow based on one-dimensional turbulence modeling, *Comput. Methods Appl. Mech. Engrg.* 199 (2010) 865–880.
- [23] S. Wunsch, A.R. Kerstein, A stochastic model for high-Rayleigh-number convection, *J. Fluid Mech.* 528 (2005) 173–205.
- [24] T. Echekki, A.R. Kerstein, T.D. Dreeben, J.-Y. Chen, ‘One-dimensional turbulence’ simulation of turbulent jet diffusion flames: Model formulation and illustrative applications, *Combust. Flame* 125 (2001) 1083–1105.
- [25] B. Ranganath, T. Echekki, An ODT-based closure model in non-premixed combustion, *Prog. Comput. Fluid Dynam.* 6 (2006) 409–418.
- [26] J. Hewson, A. Kerstein, Local extinction and reignition in nonpremixed turbulent CO/H₂/N₂ jet flames, *Combust. Sci. Technol.* 174 (2002) 35–66.
- [27] J. Hewson, A. Kerstein, Stochastic simulation of transport and chemical kinetics in turbulent CO/H₂/N₂ flames, *Combust. Theo. Model.* 5 (2001) 669.
- [28] Z. Jozefik, A.R. Kerstein, H. Schmidt, S. Lyra, H. Kolla, J.H. Chen, One-dimensional turbulence modeling of a turbulent counterflow flame with comparison to DNS, *Combust. Flame* 162 (2015) 2999–3015.
- [29] Z. Jozefik, A.R. Kerstein, H. Schmidt, Simulation of shock-turbulence interaction in non-reactive flow and in turbulent deflagration and detonation regimes using one-dimensional turbulence, *Combust. Flame* 164 (2016) 53–67.
- [30] D.O. Lignell, D.S. Rappleye, One-dimensional-turbulence simulation of flame extinction and reignition in planar ethylene jet flames, *Combust. Flame* 159 (2012) 2930–2943.
- [31] C. Xu, A.Y. Poludnenko, X. Zhao, H. Wang, T. Lu, Structure of strongly turbulent premixed n-dodecane-air flames: Direct numerical simulations and chemical explosive mode analysis, *Combust. Flame* 209 (2019) 27–40.
- [32] N. Punati, J.C. Sutherland, A.R. Kerstein, E.R. Hawkes, J.H. Chen, An evaluation of the one-dimensional turbulence model: Comparison with direct numerical simulations of CO/H₂ jets with extinction and reignition, *Proc. Combust. Inst.* 33 (2011) 1515–1522.
- [33] Q. Ni, Y. Shi, S. Chen, Statistics of one-dimensional compressible turbulence with random large-scale force, *Phys. Fluids* 25 (2013) 075106.
- [34] D.G. Goodwin, H.K. Moffat, I. Schoegl, R.L. Speth, B.W. Weber, Cantera: An object-oriented software toolkit for chemical kinetics, thermodynamics, and transport processes, 2022, <http://dx.doi.org/10.5281/zenodo.6387882>, Version 2.6.0, <https://www.cantera.org>.
- [35] D. Lignell, A. Kerstein, G. Sun, E. Monson, Mesh adaption for efficient multiscale implementation of one-dimensional turbulence, *Theor. Comput. Fluid Dyn.* 27 (2013) 273–295.
- [36] A.C. Hindmarsh, P.N. Brown, K.E. Grant, S.L. Lee, R. Serban, D.E. Shumaker, C.S. Woodward, SUNDIALS: Suite of nonlinear and differential/algebraic equation solvers, *ACM Trans. Math. Softw.* 31 (2005) 363–396.
- [37] Y. Tao, G.P. Smith, H. Wang, Critical kinetic uncertainties in modeling hydrogen/carbon monoxide, methane, methanol, formaldehyde, and ethylene combustion, *Combust. Flame* 195 (2018) 18–29.
- [38] G.P. Smith, Y. Tao, H. Wang, Foundational fuel chemistry model version 1.0 (FFCM-1), 2016, <https://web.stanford.edu/group/haiwanglab/FFCM1/pages/FFCM1.html>.
- [39] X. Zheng, T. Lu, C. Law, Experimental counterflow ignition temperatures and reaction mechanisms of 1, 3-butadiene, *Proc. Combust. Inst.* 31 (2007) 367–375.
- [40] A.Y. Poludnenko, E.S. Oran, The interaction of high-speed turbulence with flames: Global properties and internal flame structure, *Combust. Flame* 157 (2010) 995–1011.
- [41] P.E. Hamlington, A.Y. Poludnenko, E.S. Oran, Interactions between turbulence and flames in premixed reacting flows, *Phys. Fluids* 23 (2011) 125111.
- [42] P.E. Hamlington, A.Y. Poludnenko, E.S. Oran, Intermittency in premixed turbulent reacting flows, *Phys. Fluids* 24 (2012) 075111.
- [43] C.A. Towery, A.Y. Poludnenko, P.E. Hamlington, Detonation initiation by compressible turbulence thermodynamic fluctuations, *Combust. Flame* 213 (2020) 172–183.
- [44] A.Y. Poludnenko, E.S. Oran, The interaction of high-speed turbulence with flames: Turbulent flame speed, *Combust. Flame* 158 (2011) 301–326.
- [45] A.Y. Poludnenko, T.A. Gardiner, E.S. Oran, Spontaneous transition of turbulent flames to detonations in unconfined media, *Phys. Rev. Lett.* 107 (2011) 054501.
- [46] A.Y. Poludnenko, Pulsating instability and self-acceleration of fast turbulent flames, *Phys. Fluids* 27 (2015) 014106.
- [47] A.Y. Poludnenko, J. Chambers, K. Ahmed, V.N. Gamezo, B.D. Taylor, A unified mechanism for unconfined deflagration-to-detonation transition in terrestrial chemical systems and type Ia supernovae, *Science* 366 (2019) 6465.
- [48] Y. Kozak, S.S. Dammati, L.G. Bravo, P.E. Hamlington, A.Y. Poludnenko, WENO interpolation for Lagrangian particles in highly compressible flow regimes, *J. Comput. Phys.* 402 (2020) 109054.
- [49] S.S. Dammati, Y. Kozak, C. Rising, J. Reyes, K. Ahmed, A.Y. Poludnenko, Numerical investigation of the accuracy of particle image velocimetry technique in gas-phase detonations, *Proc. Combust. Inst.* 38 (2021) 3671–3681.
- [50] T.A. Gardiner, J.M. Stone, An unsplit Godunov method for ideal MHD via constrained transport in three dimensions, *J. Comput. Phys.* 227 (2008) 4123–4141.
- [51] A. Khokhlov, J. Austin, F. Pintgen, J. Shepherd, Numerical study of the detonation wave structure in ethylene-oxygen mixtures, in: 42nd AIAA Aerospace Sciences Meeting and Exhibit, 2004, p. 792.
- [52] G. Strang, On the construction and comparison of difference schemes, *SIAM J. Numer. Anal.* 5 (1968) 506–517.
- [53] R.J. Kee, F.M. Rupley, E. Meeks, J.A. Miller, CHEMKIN-III: A Fortran Chemical Kinetics Package for the Analysis of Gas-Phase Chemical and Plasma Kinetics, Tech. Rep. Sandia National Laboratories Report SAND-96-8216, Sandia National Laboratories, Livermore, CA, 1996.
- [54] F. Perini, E. Galligani, R.D. Reitz, An analytical Jacobian approach to sparse reaction kinetics for computationally efficient combustion modeling with large reaction mechanisms, *Energy Fuels* 26 (2012) 4804–4822.
- [55] J.O. Hirschfelder, C.F. Curtiss, R.B. Bird, *The Molecular Theory of Gases and Liquids*, Wiley, New York, 1964.
- [56] J. Warnatz, Influence of transport models and boundary conditions on flame structure, in: *Numerical Methods in Laminar Flame Propagation*, Springer, 1982, pp. 87–111.
- [57] A. Ern, V. Giovangigli, *Multicomponent Transport Algorithms*, vol. 24, Springer Science & Business Media, 1994.
- [58] R.J. Kee, G. Dixon-Lewis, J. Warnatz, M.E. Coltrin, J.A. Miller, A Fortran Computer Code Package for the Evaluation of Gas-Phase Multicomponent Transport Properties, Tech. Rep. Sandia National Laboratories Report SAND86-8246, Sandia National Laboratories, Livermore, CA, 1986.
- [59] A. Aspden, M. Day, J. Bell, Towards the distributed burning regime in turbulent premixed flames, *J. Fluid Mech.* 871 (2019) 1–21.
- [60] R.J. Kee, J.F. Grcar, M.D. Smooke, J.A. Miller, E. Meeks, PREMIX: A Fortran Program for Modeling Steady Laminar One-Dimensional Premixed Flames, Tech. Rep. Sandia National Laboratories Report SAND85-824, Sandia National Laboratories, Livermore, CA, 1985.

- [61] M. Fistler, A. Kerstein, D.O. Lignell, M. Oevermann, Turbulence modulation in particle-laden stationary homogeneous isotropic turbulence using one-dimensional turbulence, *Phys. Rev. Fluids* 5 (2020) 044308.
- [62] R. Abdel-Gayed, D. Bradley, M. Hamid, M. Lawes, Lewis number effects on turbulent burning velocity, in: *Symp. (Int.) Combust.*, vol. 20, Elsevier, 1985, pp. 505–512.
- [63] T.M. Wabel, A.W. Skiba, J.F. Driscoll, Turbulent burning velocity measurements: Extended to extreme levels of turbulence, *Proc. Combust. Inst.* 36 (2017) 1801–1808.
- [64] J. Jayachandran, R. Zhao, F.N. Egolfopoulos, Determination of Laminar flame speeds using stagnation and spherically expanding flames: Molecular transport and radiation effects, *Combust. Flame* 161 (2014) 2305–2316.
- [65] A. Aspden, M. Day, J. Bell, Turbulence–flame interactions in lean premixed hydrogen: Transition to the distributed burning regime, *J. Fluid Mech.* 680 (2011) 287–320.
- [66] M.S. Day, J.B. Bell, Numerical simulation of Laminar reacting flows with complex chemistry, *Combust. Theo. Model.* 4 (2000) 535.
- [67] A. Aspden, M. Day, J. Bell, Lewis number effects in distributed flames, *Proc. Combust. Inst.* 33 (2011) 1473–1480.
- [68] A.R. Kerstein, Linear-eddy modeling of turbulent transport. II: Application to shear layer mixing, *Combust. Flame* 75 (1989) 397–413.
- [69] G. Sun, D.O. Lignell, J.C. Hewson, C.R. Gin, Particle dispersion in homogeneous turbulence using the one-dimensional turbulence model, *Phys. Fluids* 26 (2014) 103301.
- [70] W.T. Ashurst, A.R. Kerstein, Erratum:“one-dimensional turbulence: Variable-density formulation and application to mixing layers”[*phys. Fluids* 17, 025107 (2005)], *Phys. Fluids* 21 (2009) 119901.
- [71] Z. Jozefik, A.R. Kerstein, H. Schmidt, Towards a compressible reactive multiscale approach based on one-dimensional turbulence, in: *Active Flow and Combustion Control* 2014, Springer, 2015, pp. 197–211.
- [72] D.O. Lignell, V.B. Lansinger, J. Medina, M. Klein, A.R. Kerstein, H. Schmidt, M. Fistler, M. Oevermann, One-dimensional turbulence modeling for cylindrical and spherical flows: Model formulation and application, *Theor. Comput. Fluid Dyn.* 32 (2018) 495–520.
- [73] V. Eswaran, S.B. Pope, An examination of forcing in direct numerical simulations of turbulence, *Comput. & Fluids* 16 (1988) 257–278.
- [74] G. Mallouppas, W. George, B. van Wachem, New forcing scheme to sustain particle-laden homogeneous and isotropic turbulence, *Phys. Fluids* 25 (2013) 083304.